A 70-V INTEGRATED SSHC RECTIFIER FOR TRIBOELECTRIC ENERGY HARVESTING WITH DUTY-CYCLE-BASED MPPT

Wenyu Peng

A 70-V INTEGRATED SSHC RECTIFIER FOR TRIBOELECTRIC ENERGY HARVESTING WITH DUTY-CYCLE-BASED MPPT

Thesis

To obtain the degree of Master of Science
in Electrical Engineering, Department of Microelectronics,
Delft University of Technology, Delft, the Netherlands,
to be defended on 28th February, 2023,

by

Wenyu Peng

Department of microelectronics,
Faculty of Electrical Engineering, Mathematics, and Computer Science,
Delft University of Technology, the Netherlands

Supervisor: dr. Sijun Du
Daily supervisor: Xinling Yue

Thesis Committee:

Dr. Dante Muratore,	Bioelectronics, Microelectronics, EEMCS
Dr. Sijun Du,	Electronic Instrumentation, Microelectronics, EEMCS

An electronic version of this dissertation is available at
http://repository.tudelft.nl/.

ABSTRACT

A triboelectric nanogenerator (TENG) is a new transducer utilizing contact electrification and electrostatic induction to transduce mechanical energy into electric energy. Due to its high energy density and flexibility, it can be employed to make electronic devices self-powered by ambient mechanical energy in many application scenarios, such as biomedical devices, wearable electronics, and Internet-of-Things (IoT) sensors. However, it is challenging to extract electrical energy from TENG due to its time-varying and low internal capacitance. IC technology is advantageous in triboelectric energy harvesting (TEH) and power management with low leakage current and active harvesting configurations. Currently, studies on dedicated integrated power conversion techniques are very limited. Due to the exponentially increasing research interests in TENG, a comprehensive study on the TENG energy harvesting system, emphasizing IC power conversion techniques, is urgently needed.

Therefore, this project contains two parts. The first part is summarizing and comparing the state-of-the-art in TEH, as well as the advanced techniques employed in other kinetic energy harvesting such as piezoelectric and electrostatic energy harvesting. The potential of mature IC energy extraction techniques in TEH is emphasized. This part of work is collected and summarized in a literature review, which is being reviewed by IEEE Transactions on Circuit and System: I. For the rest of this thesis, a dedicated TEH interface employing Synchronized-Switch harvesting on Capacitor (SSHC) and Maximum Power Point Tracking (MPPT) working at 70 V is proposed, with theoretical analysis, design details, and simulated performance elaborated in this thesis. This is the first fully-integrated active rectifier reported for TEH. It is going to be fabricated on April 2023.

ACKNOWLEDGEMENTS

First of all, I would like to give my sincere gratitude to my supervisor, dr. Sijun Du. He teaches me with patience, and always encourages me and inspires me. Besides, he offers me a PhD position so that I could keep working on this project and make efforts to the development of IC society.

Secondly, I would like to acknowledge my friends for their love and support. It can be difficult to live in a country far from my hometown without their company. During these two years, I have enjoyed a wonderful life with my friends. It is a good memory of traveling to many places and countries with you. Besides, my old friends studying or working in China, England and US usually contact me. Friendship is the best fortune I have ever had.

Last but not least, I want to thank my parents. No matter when and where I am, I know that they will respond to me and give me anything regardless of the cost. They are the most reliable and solid backup to me.

CONTENTS

1

INTRODUCTION

1.1. BACKGROUND

Electronic devices are widely used to make people's life and work easier. With the development of integrated circuits (IC) and microelectromechanical systems (MEMS), functional electronic systems can be integrated into single pieces of Silicon with ultra-small form factors, higher energy efficiency, and better performance. However, a stable power supply is essential for all electronic devices. Nowadays, most autonomous systems are powered by batteries. Despite the high power density of batteries, they usually dominate the size of electronic devices. Besides, the batteries will eventually run out of energy one day and they have to be charged or replaced. Unfortunately, in many application scenarios, it is extremely difficult, or even impossible, to charge or replace the batteries, e.g., biomedical implants and ubiquitously distributed Internet-of-Things (IoT) sensors. Furthermore, batteries can also bring pollution to the environment. Thus, battery-free systems have drawn much research interest in the past decade with energy harvesting technology, which harvests ambient sustainable energy and converts it into usable electrical form. So far, various energy forms can be harvested thanks to the exploration of the corresponding energy transducers, such as photoelectric, thermoelectric, and mechano-electrical transducers.

Amongst these energy sources, mechanical energy exists almost everywhere. In past decades, piezoelectric energy harvesting and electrostatic energy harvesting were popular techniques for harvesting mechanical energy. They transduce mechanical movement/vibration into electricity relying on the vibration of internal cantilevers or plates. Consequently, they can only provide high output power with periodic and stable mechanical vibration. However, many mechanical movements, such as human motions and tides, are irregular and unpredictable, which lead to extremely low efficiency if using piezoelectric and electrostatic energy harvesters. To harvest mechanical energy in a much broader extent, a new mechanoelectrical transducer was proposed recently: the triboelectric nanogenerator (TENG).

A TENG works based on triboelectrification (contact electrification phenomenon) and electrostatic induction. Triboelectrification refers to the redistribution of electric

1

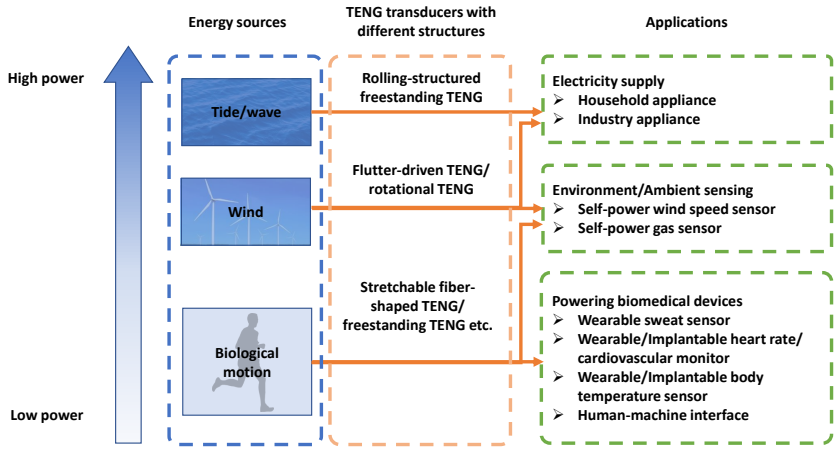

Figure 1.1: The energy sources to be harvested by different structures of TENG in various application scenarios

charges between two different substances when they are squeezed or rubbed against each other. When the distance or contact area between them changes, an electric potential will be induced due to the displacement current. This indicates the potential of triboelectrification in sensing displacement and transducing mechanical energy to electric energy.

The first TENG was proposed in 2012 [1]. In recent years, the research interest in triboelectric energy harvesting has been exponentially increasing [2]. TENG is advantageous in high flexibility and energy density, which makes it more suitable for miniaturization and planarization compared to piezoelectric and electrostatic energy harvesters [3]–[5]. Additionally, different from piezoelectric and electromagnetic kinetic energy harvesting, triboelectric energy harvesting is not limited by the resonant frequency and thus can transduce more power at low and non-periodic vibration frequency [6], [7]. As a consequence, it has been experimentally validated to harvest mechanical energy from the human body when embedded in textile [8], or bracelet [9], [10], or even from the motion of organs [11] to provide a stable power supply to low-power wearable or implantable devices, such as IoT environment monitors [12], health monitors [13]–[18], and human-machine interfaces [19]–[21]. Furthermore, the feasibility of TENG in harvesting tide energy, wave energy [22], [23] and wind energy [24], [25] has been exploited. The applications of TENG working as a kinetic energy transducer are presented in Fig. 1.1, which also includes the energy sources and feasible structures.

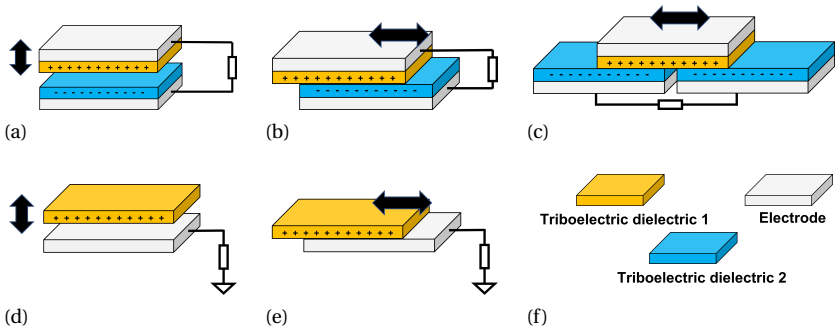

Figure 1.2: Two electrode configurations for TENGs in different working modes: double-electrode configuration in (a) vertical contact-separation mode, (b) lateral-sliding mode, and (c) freestanding mode; Single-electrode configuration in (d) vertical contact-separation mode, and (e) lateral-sliding mode [27]. (f) Figure legends.

1.2. FUNDAMENTAL THEORIES OF TENG

1.2.1. STRUCTURES

The triboelectrification phenomenon generates static electricity on dielectric, whose polarity and quantity are determined by electron affinities of materials [26], [27]. The displacement of charges generates electrical potential, which contains energy to be harvested and utilized. Typically, a TENG has three working modes: vertical contact-separation mode, lateral-sliding mode, and freestanding mode. Besides, there are two electrode configurations: single-electrode and double-electrode [27]. The combinations of different working modes and electrode configurations are illustrated in Fig. 1.2.

The vertical contact-separation mode has two dielectrics, or one dielectric and one electrode plate, moving face to face as presented in Fig. 1.2a and Fig. 1.2d. Triboelectrification occurs when they are in contact and squeezed. When two plates move away from each other, a voltage potential difference is induced between them by the displacement current. In lateral-sliding and freestanding mode, the plates can have rotational or translational movement with the triboelectricity generated by rubbing [28]. For the double-electrode configurations presented in Fig. 1.2b and Fig. 1.2c, when the effective contact area between dielectrics changes, the charge on the non-overlapping region induces different potentials on the anode and cathode electrode plates. While for the single-electrode lateral-sliding TENG illustrated in Fig. 1.2e, the potential is induced by the charge on the dielectric at the overlapping area between the dielectric and the electrode. With the lateral-sliding and freestanding TENG, the kinetic energy in the parallel relative motion can be harvested. For single electrode configurations, the current flows between electrode and ground, so the ground can be set as either anode or cathode in this case [27].

In the rest of this section, the double-electrode configuration will be taken as an example for theoretical analysis, but both single- and double-electrode configurations have similar properties.

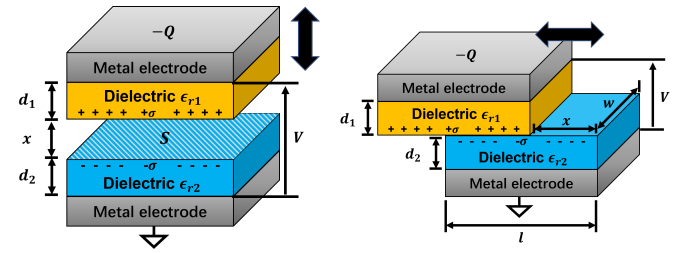

Figure 1.3: The theoretical model of (a) the double-electrode vertical contact-separation TENG and (b) the double-electrode lateral-sliding TENG with significant parameters labeled [29], [32].

1.2.2. FEATURE ANALYSIS AND MODELING

To design energy harvesting circuits for a TENG, the characteristics of current and voltage generated from it must be taken into consideration. The real-time output of a TENG can be comprehensively described by the V-Q-x relationship with three variables: the voltage between electrodes V, the generated charge Q, and the relative displacement between the plates x [29]. Since the TENG in contact-separation mode and sliding mode have different characteristics, they should be analyzed separately. First, the V-Q-x relationship of the vertical contact-separation TENG is elucidated. Based on its working mechanism, it can be approximately considered as a variable capacitor with a uniform electric field between plate electrodes [30], [31]. Thus, the induced V is derived by the product of x and the electric field intensity mathematically. The internal electric field of TENG is the superposition of two electric fields, induced by the triboelectric charge and the Q on the electrode plates respectively. Therefore, the V-Q-x relationship of the vertical contact-separation TENG can be derived by the following equation:

$$V = -\frac{Q}{S\epsilon_0}\left(\frac{d_1}{\epsilon_{r1}} + \frac{d_2}{\epsilon_{r2}} + x\right) + \frac{\sigma x}{\epsilon_0} \tag{1.1}$$

where:

S is the plate size;

ϵ_0 is the vacuum permittivity.

d_1 and d_2 are the thicknesses of dielectric layers;

ϵ_{r1} and ϵ_{r2} are the relative dielectric permittivity of each dielectric layer;

σ is the surface charge density of the dielectric generated by the triboelectrification;

These variables and parameters are labeled in Fig. 1.3a. Regarding single-electrode contact-separation TENGs, Eq. 1.1 also works except that only one dielectric layer exists; hence, one of the d_1 and d_2 should be set 0. Eq. 1.1 can also be expressed in another form:

$$V = -\frac{Q}{C_{TENG}} + V_{OC} \tag{1.2}$$

where,

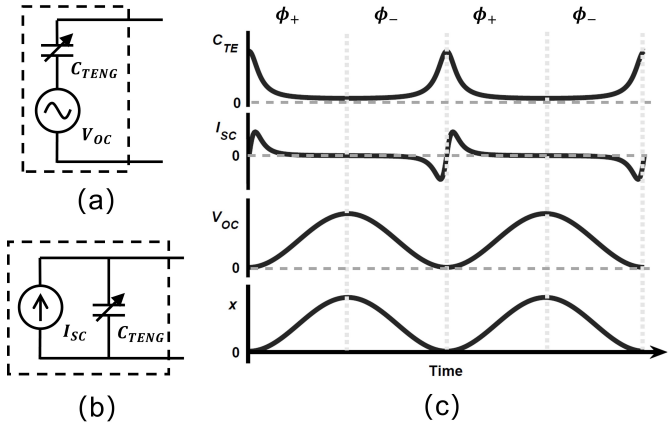

Figure 1.4: (a) The theoretical equivalent voltage source model and (b) the theoretical equivalent current source model of TENG [33]. (c) The waveform of the real-time internal capacitance (C_{TE}), a current source (I_{SC}), and a voltage source (V_{OC}) is illustrated when TENG operates in sinusoidal vibration (x).

$$C_{TENG} = \frac{S\epsilon_0}{d_0 + x} \qquad (d_0 = \frac{d_1}{\epsilon_{r1}} + \frac{d_2}{\epsilon_{r2}}) \tag{1.3}$$

$$V_{OC} = \frac{\sigma x}{\epsilon_0} \tag{1.4}$$

Another important parameter of TENG in analyzing the energy extraction efficiency is the maximal charge output, i.e., the total output charge under short-circuit condition in each semi-cycle, denoted as Q_{SC}. Its relationship with x is derived from Eq. 1.1 with $V = 0$ and expressed as:

$$Q_{SC} = \frac{S\sigma x}{d_0 + x} \tag{1.5}$$

Eq. 1.2 is derived from an electronic perspective of a vertical contact-separation TENG, i.e., an equivalent circuit model composed of a voltage source that is identical to the potential induced by the electrostatic surface charge, i.e., the open-circuit voltage of TENG V_{OC}, and an inherent capacitor with a variable capacitance C_{TENG} connected in series [33]. This model is illustrated in Fig. 1.4(a), with the expression of V_{OC} and C_{TENG} presented by Eq. 1.3 and Eq. 1.4 respectively. Besides, the waveform of V_{OC} and C_{TENG} is illustrated in Fig. 1.4(c) when TENG operates in sinusoidal vibration. It is advantageous in its direct relationship with the physical mechanism of TENG, as well as the linearity between the V_{OC} and x.

According to Norton's theorem, this model can be transformed into a current source, which is identical to the short-circuit output current I_{SC}, in parallel with the internal impedance, as presented in Fig. 1.4(b). Due to the time-varying capacitance C_{TENG}, the expression of I_{SC} with respect to the displacement of TENG will be complicated.

Nevertheless, this model is advantageous in analyzing the phase difference between the output voltage and current, and thus is commonly utilized in active energy extractor design.

One problem with the V-Q-x relationship of the TENG shown in Eq. 1.1 is that this equation is not always valid when x approaches or exceeds the width of the dielectric. In that case, the electric field becomes nonuniform, and the induced potential becomes nonlinear to x [31]. In practice, when x exceeds a certain threshold, the increase of V_{OC} cannot match the decrease of C_{TENG}; hence the voltage across the TENG will drop, or invert if the TENG is in a loop. The specific relationship between V_{OC} and x under this condition is complicated and influenced by many factors, such as the shape and width of the dielectric, etc. In practice, this situation can be avoided with several methods. The first method is to assume that the V_{OC} stays unchanged when x exceeds a certain threshold in simulations. This is the most convenient method but can be inaccurate and may lead to unexpected output, such as voltage drop or inversion. Another method is to limit the displacement of TENG in both simulation and practice. This solution guarantees consistency between simulation and experiment but is not always practical.

Then, the V-Q-x relationship of lateral-sliding TENG will be introduced. The freestanding TENG has a similar property to the lateral-sliding TENG so they share the same relationship. Despite different motion modes, the Eq. 1.2 is still valid in this mode, which means that the equivalent circuit models presented in Fig. 1.4 also work in lateral-sliding TENG. However, the parameters C_{TENG} and V_{OC} of it as well as Q_{SC} are different from those of vertical contact-separation TENG aforementioned, which are supposed to be

$$C_{TENG} = \frac{\epsilon_0 w(l-x)}{d_0} \qquad (d_0 = \frac{d_1}{\epsilon_{r1}} + \frac{d_2}{\epsilon_{r2}}) \tag{1.6}$$

$$V_{OC} = \frac{\sigma x}{\epsilon_0 (l-x)} d_0 \tag{1.7}$$

$$Q_{SC} = \sigma w x \tag{1.8}$$

where l and w denote the length and width of the plate respectively. All symbols represent the same parameters as those in the contact-separation TENG and are labeled in the theoretical model illustrated in Fig.1.3b [32]. These equations are valid when x is smaller than l. When x is larger than l, the V_{OC} is not related to the displacement but only determined by the electrostatic surface charge induced by the triboelectric effect. In lateral-sliding and freestanding TENGs, the I_{SC} of the current source model is linear to the x. However, as it is still not always equal to the current from the source, the voltage source model is recommended in lateral-sliding TENGs as well.

Inspired by the V-Q-x relationship, the V-Q plot has been utilized to analyze the TENG output [34]. An example of the V-Q plot is illustrated in Fig. 1.5. The V axis represents the voltage across the TENG while the Q axis represents the output charge. V_{OC+} is identical to V_{OC} at the maximum displacement, and the Q_{SC+} is the total charge output on that condition. V_{OC-} is identical to the voltage across the internal capacitor when the charge on that is equal to Q_{SC+} and the capacitance C_{TENG} reaches the maximum. In this case, the slope of the dashed lines connecting $(0, V_{OC+})$ and $(Q_{SC+}, 0)$ is the reciprocal of the minimal C_{TENG}, while that connecting origin and the point (Q_{SC+}, V_{OC-}) is

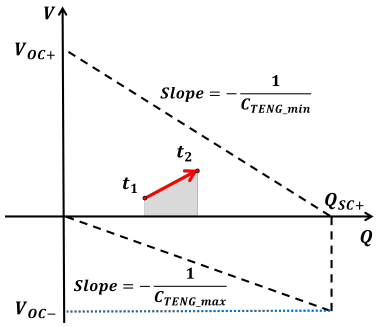

Figure 1.5: The V-Q plot of TENG.

the reciprocal of the maximal C_{TENG} as presented in Fig. 1.5. The output energy can be calculated by the following equation:

$$E = \int VIdt = \int VdQ \tag{1.9}$$

Eq. 1.9 indicates that the output energy can be conveniently represented by an area in the V-Q plot. As illustrated in Fig. 1.5, when TENG works from t_1 to t_2, the energy output is represented by the shadow area and thus can be calculated mathematically. Therefore, the V-Q plot is useful in triboelectric energy harvesting design to calculate energy extraction performance.

1.3. EXPERIMENTAL VALIDATION

To validate the characteristics of TENG, a prototype is fabricated to determine the parameters of TENG model employed in circuit design. I made a PTFE-Al contact-separation TENG which is typically used for measurement in many works. The triboelectric layers consist of PTFE (Teflon) film and Aluminum film. The former has a strong negative charging capacity while the latter has a positive charging capacity, thus they could generate more static charge than using two materials with the same triboelectric polarity. They are attached to two $4 \times 4cm$ raw PCBs with single-side copper respectively, as presented in Fig. 1.6a. The copper films are utilized as electrodes while the insulating substrate of PCB seals and protects the transducer. Then, both boards are fixed on 3D-printed platforms and excited by a shaker to do the contact-separation movement as depicted by Fig. 1.6b. If the shaker operates in sinusoidal vibration, the output voltage waveform of TENG is expected to be sinusoidal according to Eq.1.4.

The next step is to measure the characteristics of this prototype i.e., its open-circuit voltage and internal capacitance. Due to the small internal capacitance and high open-circuit voltage of TENG, the normal oscilloscope probe can hardly measure the voltage directly since its internal impedance is limited. Based on my measurement and the parameters on manual, the real input impedance of probe consists of a 80 pF capacitor and a $1M/10M\Omega$ resistor in parallel, while the capacitance of the in-house fabricated TENG is tens of pico-Farad. Thus I build a specified measurement circuit presented in

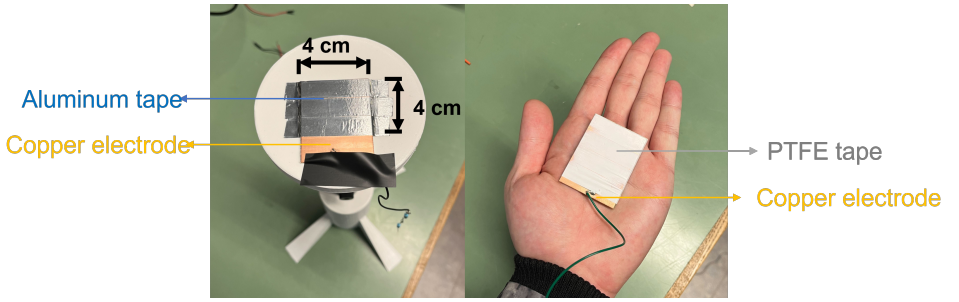

(a)

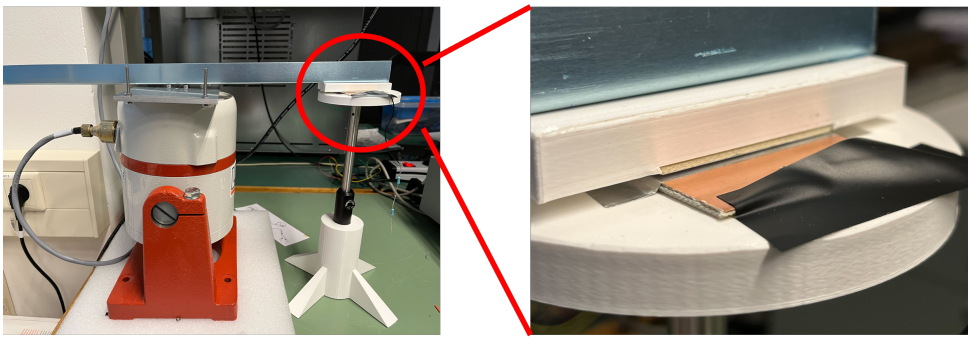

(b)

Figure 1.6: (a) The internal structure of in-house fabricated contact-separation TENG prototype; (b) TENG is excited by a shaker.

Fig. 1.7 to boost the input impedance and suppress the leakage current. When the resistor is 100$M\Omega$ and the probe is set to 10X mode (internal resistance equal to 10$M\Omega$), the output voltage waveform is close to the sinusoidal wave, with the deformation mainly caused by leakage current. The waveform is illustrated in Fig.1.8. The peak-to-peak voltage read from the pattern is approximately 5.7 V, corresponding to 63 V over TENG. Due to the leakage caused by measurement circuit, the 63 V is not the accurate open-circuit voltage of TENG.

Regarding the internal capacitance of TENG, we are interested in its maximal and minimal transient capacitance, corresponding to the moment that electrodes are the closest and furthest from each other respectively. Thus, I constitute a low-pass filter with TENG, a variable resistor and a sinusoidal signal generator connected in series. By measuring its corner frequency, the transient capacitance of TENG can be estimated, which is approximately 100 pF at maximum and 10 pF at minimum.

Additionally, to estimate the actual open-circuit voltage and the parameters of this TENG, the equivalent circuit is built in Cadence, with parameters adjusted to fit the simulated waveform to the measured one. Some parameters can be directly observed and measured, such as the displacement x and plate size S, while the static charge density σ and the thickness of dielectric layers are difficult to measure. After trial and error, the

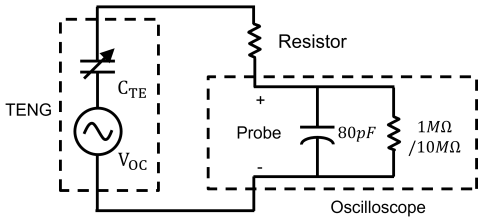

Figure 1.7: The measurement circuit to measure the output voltage of TENG.

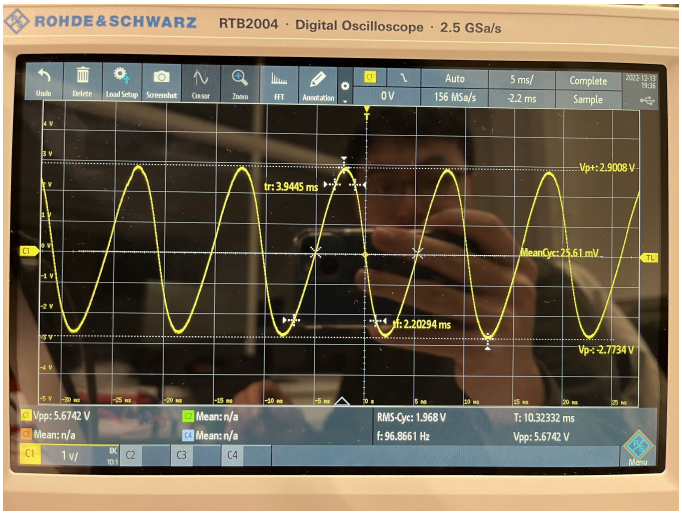

Figure 1.8: The measured open-circuit voltage of TENG.

simulation waveform is close to the measured one with the parameters presented in Table.1.1. In this case, the real peak-to-peak open-circuit voltage is approximately 170 V.

Indeed, it is reported that the charge density after triboelectric charge transfer between metal and PTFE can range from 10^{-3} to $10^{-4} C/m^2$, which is much higher than the experimental result [35]. The reason might be that the triboelectric films used in my prototype are not flat, which leads to inadequate contact with each other and thus a lower static charge density.

1.4. REQUIREMENTS FOR EXTRACTING TRIBOELECTRIC ENERGY

Based on the characteristics of TENG analyzed and measured before, some requirements for triboelectric energy harvesting can be summarized. First, if a TENG is experiencing a periodic mechanical motion, the output of the TENG is an alternating-current (AC) energy due to the internal capacitor. To make use of the harvested energy and to power load electronics, the AC energy needs to be converted to the direct-current (DC) form with a rectification technique. Different from the piezoelectric transducer and electrostatic transducer, the TENG is not typically implemented in vibration environments, which

Table 1.1: The parameters of TENG model used in the simulation

Surface charge density σ	$1.5 \times 10^{-6}\, C/m^2$
Effective contact area S	$4 \times 4\, cm^2$
Effective thickness of the triboelectric film d/ε_r	$140\, um$
Permittivity value of the air ε_0	$8.85 \times 10^{-12}\, F/m$
Maximal vibration displacement x_m	$1\, mm$

makes its output alike to a shock in a mono-directional motion cycle [36], [37]. Additionally, the voltage and current outputs are usually asymmetric for motion in different directions, even with the same distance [36], [38]. Therefore, those rectifiers applied in triboelectric energy harvesting should work with fast-changing input.

Another problem caused by the internal capacitor is that it will generate a phase difference between current and voltage outputs when the TENG is loaded capacitively. In this case, an amount of charge will be wasted to compensate for the phase delay of voltage; as a result, the energy extraction performance is degraded. In piezoelectric energy harvesting, some mature solutions to eliminate that phase difference have been proposed and employed, such as the synchronous switching techniques including synchronous electric charge extraction (SECE) technique [39] and synchronized-switch harvesting on inductor (SSHI) technique [40]. However, different from the constant internal capacitance of the piezoelectric transducer, the internal capacitance of TENG is time-varying, which limits the effectiveness of those techniques.

Besides, the internal impedance of TENG is very high due to the small internal capacitance and low operating frequency. In practice, this causes high output voltage when TENG is loaded with high resistance or in open-circuit conditions, where high voltage tolerance of devices in the interfaces is typically required. On the other hand, if the load impedance is small, the current can rocket sharply at the beginning but drop soon, and in this case, the power output is very low [41]. Therefore, to extract more energy from a TENG, the power management interface must optimize its load impedance or the rectification voltage based on the time-varying internal impedance of the transducer [42].

BIBLIOGRAPHY

[1] F.-R. Fan, Z.-Q. Tian, and Z. L. Wang, "Flexible triboelectric generator," *Nano energy*, vol. 1, no. 2, pp. 328–334, 2012, ISSN: 2211-2855.

[2] T. Cheng, Q. Gao, and Z. L. Wang, "The current development and future outlook of triboelectric nanogenerators: A survey of literature," *Advanced Materials Technologies*, vol. 4, no. 3, p. 1 800 588, 2019, ISSN: 2365-709X.

[3] J. Luo and Z. L. Wang, "Recent advances in triboelectric nanogenerator based self-charging power systems," *Energy Storage Materials*, vol. 23, pp. 617–628, 2019, ISSN: 2405-8297.

[4] C. Wu, A. C. Wang, W. Ding, H. Guo, and Z. L. Wang, "Triboelectric nanogenerator: A foundation of the energy for the new era," *Advanced Energy Materials*, vol. 9, no. 1, p. 1 802 906, 2019, ISSN: 1614-6832. DOI: https://doi.org/10.1002/aenm.201802906. [Online]. Available: https://doi.org/10.1002/aenm.201802906.

[5] Y. Wang, Y. Yang, and Z. L. Wang, "Triboelectric nanogenerators as flexible power sources," *npj Flexible Electronics*, vol. 1, no. 1, pp. 1–10, 2017, ISSN: 2397-4621.

[6] Z. L. Wang, T. Jiang, and L. Xu, "Toward the blue energy dream by triboelectric nanogenerator networks," *Nano Energy*, vol. 39, pp. 9–23, 2017, ISSN: 2211-2855.

[7] J. Zhao, G. Zhen, G. Liu, *et al.*, "Remarkable merits of triboelectric nanogenerator than electromagnetic generator for harvesting small-amplitude mechanical energy," *Nano Energy*, vol. 61, pp. 111–118, 2019, ISSN: 2211-2855. DOI: https://doi.org/10.1016/j.nanoen.2019.04.047. [Online]. Available: https://www.sciencedirect.com/science/article/pii/S2211285519303489.

[8] Z. Wen, M.-H. Yeh, H. Guo, *et al.*, "Self-powered textile for wearable electronics by hybridizing fiber-shaped nanogenerators, solar cells, and supercapacitors," *Science Advances*, vol. 2, no. 10, e1600097, 2016. DOI: 10.1126/sciadv.1600097. [Online]. Available: https://doi.org/10.1126/sciadv.1600097.

[9] Y. Song, H. Wang, X. Cheng, *et al.*, "High-efficiency self-charging smart bracelet for portable electronics," *Nano Energy*, vol. 55, pp. 29–36, 2019, ISSN: 2211-2855.

[10] K. Parida, J. Xiong, X. Zhou, and P. S. Lee, "Progress on triboelectric nanogenerator with stretchability, self-healability and bio-compatibility," *Nano Energy*, vol. 59, pp. 237–257, 2019, ISSN: 2211-2855.

[11] S. Zhang, M. Bick, X. Xiao, G. Chen, A. Nashalian, and J. Chen, "Leveraging triboelectric nanogenerators for bioengineering," *Matter*, vol. 4, no. 3, pp. 845–887, 2021, ISSN: 2590-2385.

[12] Y. Su, G. Xie, H. Tai, *et al.*, "Self-powered room temperature no2 detection driven by triboelectric nanogenerator under uv illumination," *Nano Energy*, vol. 47, pp. 316–324, 2018, ISSN: 2211-2855.

[13] Y. Song, J. Min, Y. Yu, *et al.*, "Wireless battery-free wearable sweat sensor powered by human motion," *Sci Adv*, vol. 6, no. 40, eaay9842, 2020, ISSN: 2375-2548 (Electronic) 2375-2548 (Linking). DOI: 10.1126/sciadv.aay9842. [Online]. Available: https://www.ncbi.nlm.nih.gov/pubmed/32998888.

[14] T. Tat, A. Libanori, C. Au, A. Yau, and J. Chen, "Advances in triboelectric nanogenerators for biomedical sensing," *Biosensors and Bioelectronics*, p. 112 714, 2020, ISSN: 0956-5663.

[15] Q. Zheng, B. Shi, F. Fan, *et al.*, "In vivo powering of pacemaker by breathing-driven implanted triboelectric nanogenerator," *Advanced Materials*, vol. 26, no. 33, pp. 5851–5856, 2014, ISSN: 0935-9648. DOI: https://doi.org/10.1002/adma.201402064. [Online]. Available: https://doi.org/10.1002/adma.201402064.

[16] Y. Fang, Y. Zou, J. Xu, *et al.*, "Ambulatory cardiovascular monitoring via a machine-learning-assisted textile triboelectric sensor," *Advanced Materials*, vol. 33, no. 41, p. 2 104 178, 2021, ISSN: 0935-9648.

[17] Z. Li, K. Hu, M. Yang, *et al.*, "Elastic cu@ppy sponge for hybrid device with energy conversion and storage," *Nano Energy*, vol. 58, pp. 852–861, 2019, ISSN: 2211-2855. DOI: https://doi.org/10.1016/j.nanoen.2018.11.093. [Online]. Available: https://www.sciencedirect.com/science/article/pii/S2211285519301041.

[18] Z. Li, Q. Zheng, Z. L. Wang, and Z. Li, "Nanogenerator-based self-powered sensors for wearable and implantable electronics," *Research*, vol. 2020, 2020.

[19] W. Ding, A. C. Wang, C. Wu, H. Guo, and Z. L. Wang, "Human–machine interfacing enabled by triboelectric nanogenerators and tribotronics," *Advanced Materials Technologies*, vol. 4, no. 1, p. 1 800 487, 2019, ISSN: 2365-709X.

[20] P. Tan, Q. Zheng, Y. Zou, *et al.*, "A battery-like self-charge universal module for motional energy harvest," *Advanced Energy Materials*, vol. 9, no. 36, p. 1 901 875, 2019, ISSN: 1614-6832. DOI: https://doi.org/10.1002/aenm.201901875. [Online]. Available: https://doi.org/10.1002/aenm.201901875.

[21] J. Xue, Y. Zou, Y. Deng, and Z. Li, "Bioinspired sensor system for health care and human-machine interaction," *EcoMat*, vol. 4, no. 5, e12209, 2022, ISSN: 2567-3173. DOI: https://doi.org/10.1002/eom2.12209. [Online]. Available: https://doi.org/10.1002/eom2.12209.

[22] X. Wang, S. Niu, Y. Yin, F. Yi, Z. You, and Z. L. Wang, "Triboelectric nanogenerator based on fully enclosed rolling spherical structure for harvesting low-frequency water wave energy," *Advanced Energy Materials*, vol. 5, no. 24, p. 1 501 467, 2015, ISSN: 1614-6832. DOI: https://doi.org/10.1002/aenm.201501467. [Online]. Available: https://doi.org/10.1002/aenm.201501467.

[23] Z. Lin, B. Zhang, H. Guo, *et al.*, "Super-robust and frequency-multiplied triboelectric nanogenerator for efficient harvesting water and wind energy," *Nano Energy*, vol. 64, p. 103 908, 2019, ISSN: 2211-2855.

[24] B. Chen, Y. Yang, and Z. L. Wang, "Scavenging wind energy by triboelectric nanogenerators," *Advanced Energy Materials*, vol. 8, no. 10, p. 1 702 649, 2018, ISSN: 1614-6832.

[25] Z. Ren, L. Wu, Y. Pang, W. Zhang, and R. Yang, "Strategies for effectively harvesting wind energy based on triboelectric nanogenerators," *Nano Energy*, vol. 100, p. 107 522, 2022, ISSN: 2211-2855. DOI: https://doi.org/10.1016/j.nanoen.2022.107522. [Online]. Available: https://www.sciencedirect.com/science/article/pii/S2211285522005997.

[26] R. Dharmasena and S. Silva, "Towards optimized triboelectric nanogenerators," *Nano Energy*, vol. 62, pp. 530–549, 2019, ISSN: 2211-2855.

[27] W.-G. Kim, D.-W. Kim, I.-W. Tcho, J.-K. Kim, M.-S. Kim, and Y.-K. Choi, "Triboelectric nanogenerator: Structure, mechanism, and applications," *ACS nano*, vol. 15, no. 1, pp. 258–287, 2021, ISSN: 1936-0851.

[28] P. Bai, G. Zhu, Y. Liu, *et al.*, "Cylindrical rotating triboelectric nanogenerator," *ACS nano*, vol. 7, no. 7, pp. 6361–6366, 2013, ISSN: 1936-0851.

[29] S. Niu, S. Wang, L. Lin, *et al.*, "Theoretical study of contact-mode triboelectric nanogenerators as an effective power source," *Energy & Environmental Science*, vol. 6, no. 12, pp. 3576–3583, 2013.

[30] R. D. I. G. Dharmasena, K. Jayawardena, C. Mills, *et al.*, "Triboelectric nanogenerators: Providing a fundamental framework," *Energy & Environmental Science*, vol. 10, no. 8, pp. 1801–1811, 2017.

[31] Q.-Z. Guo and C.-P. Liu, "Derivation of analytical equations with experimental verification for working mechanism of triboelectric nanogenerators in contact-separation mode," *Nano Energy*, vol. 76, p. 104 969, 2020, ISSN: 2211-2855.

[32] S. Niu, Y. Liu, S. Wang, *et al.*, "Theory of sliding-mode triboelectric nanogenerators," *Advanced materials*, vol. 25, no. 43, pp. 6184–6193, 2013, ISSN: 0935-9648.

[33] S. Niu, Y. S. Zhou, S. Wang, *et al.*, "Simulation method for optimizing the performance of an integrated triboelectric nanogenerator energy harvesting system," *Nano Energy*, vol. 8, pp. 150–156, 2014, ISSN: 2211-2855. DOI: https://doi.org/10.1016/j.nanoen.2014.05.018. [Online]. Available: https://www.sciencedirect.com/science/article/pii/S2211285514001025.

[34] Y. Zi, S. Niu, J. Wang, Z. Wen, W. Tang, and Z. L. Wang, "Standards and figure-of-merits for quantifying the performance of triboelectric nanogenerators," *Nature communications*, vol. 6, no. 1, pp. 1–8, 2015, ISSN: 2041-1723.

[35] S. Pan and Z. Zhang, "Fundamental theories and basic principles of triboelectric effect: A review," *Friction*, vol. 7, no. 1, pp. 2–17, 2019, ISSN: 2223-7704.

[36] P. Yingyong, P. Thainiramit, S. Nundrakwang, P. Janphuang, and D. Isarakorn, "A comparative study of the electrical characteristics of piezoelectric and triboelectric nanogenerators for energy-harvesting floor tiles," in *2020 17th International Conference on Electrical Engineering/Electronics, Computer, Telecommunications and Information Technology (ECTI-CON)*, 2020, pp. 9–12. DOI: 10.1109/ECTI-CON49241.2020.9158263.

[37] D. Kwon, G. A. Rincon-Mora, and E. O. Torres, "Harvesting ambient kinetic energy with switched-inductor converters," *IEEE Transactions on Circuits and Systems I: Regular Papers*, vol. 58, no. 7, pp. 1551–1560, 2011. DOI: 10.1109/TCSI.2011.2142731.

[38] R. Dharmasena, "Inherent asymmetry of the current output in a triboelectric nanogenerator," *Nano Energy*, vol. 76, p. 105 045, 2020, ISSN: 2211-2855.

[39] E. Lefeuvre, A. Badel, C. Richard, and D. Guyomar, "Piezoelectric energy harvesting device optimization by synchronous electric charge extraction," *Journal of Intelligent Material Systems and Structures*, vol. 16, no. 10, pp. 865–876, 2005, ISSN: 1045-389X. DOI: 10.1177/1045389X05056859. [Online]. Available: https://doi.org/10.1177/1045389X05056859.

[40] E. Lefeuvre, A. Badel, C. Richard, and D. Guyomar, "High-performance piezoelectric vibration energy reclamation," in *Smart Structures and Materials 2004: Smart Structures and Integrated Systems*, SPIE, vol. 5390, 2004, pp. 379–387.

[41] D. Zhao, X. Yu, Z. Wang, *et al.*, "Universal equivalent circuit model and verification of current source for triboelectric nanogenerator," *Nano Energy*, vol. 89, p. 106 335, 2021, ISSN: 2211-2855.

[42] S. Niu, Y. Liu, Y. S. Zhou, S. Wang, L. Lin, and Z. L. Wang, "Optimization of triboelectric nanogenerator charging systems for efficient energy harvesting and storage," *IEEE Transactions on Electron Devices*, vol. 62, no. 2, pp. 641–647, 2015, ISSN: 0018-9383.

2

REVIEW OF THE STATE-OF-THE-ARTS

Despite many studies on TENG structures and applications, few studies have been devoted to providing a comprehensive overview of the IC power conditioning circuit for triboelectric energy harvesting. Due to the increasing research interest in designing TENG-based systems, a review of the state-of-the-art IC conversion techniques and associated circuits is needed to inspire new harvesters for TENG.

2.1. PASSIVE CONVERTERS

Among all power conversion techniques, passive power converters are widely employed due to their simplicity, stability, and capability for a cold startup, though they typically suffer from low energy conversion efficiency. Passive converters are composed of passive components such as capacitors, diodes, or diode-connected transistors. The most typical passive converter is the bridge rectifier, which can be divided into two types: half-bridge rectifier (HBR) and full-bridge rectifier (FBR). Besides, rectification can be implemented together with voltage regulation via switched-capacitor technologies. A passive switched-capacitor converter, Bennet's doubler of electricity, has been reported in harvesting triboelectric and electrostatic energy as well as other power management systems. These AC-DC converters employed in triboelectric energy harvesting will be introduced respectively.

2.1.1. PASSIVE BRIDGE RECTIFIERS

Full bridge and half bridge are the two most common configurations of rectifiers. The half-bridge rectifier is composed of two diodes, where one diode allows current in one direction to pass while the other diode shorts the AC source. The full-bridge rectifier (FBR) employs two half-bridge rectifiers to regulate the current in both polarities. This configuration can rectify current regardless of its direction, so it converts more energy compared to the half-bridge configuration in one cycle and was consequently imple-

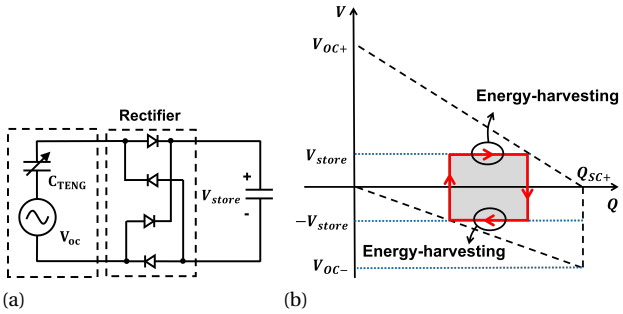

Figure 2.1: (a) The configuration and (b) V-Q plot of the standard energy harvesting circuit in triboelectric energy harvesting.

mented in many harvesters. The energy harvesting interface composed of an FBR and a rectification capacitor is named a standard energy harvesting circuit, as presented in Fig. 2.1a. When the rectification voltage i.e., the storage voltage V_{store} in this case, is fixed, the V-Q plot of a standard energy harvesting circuit in triboelectric energy harvesting is illustrated in Fig. 2.1b. The shadowed area indicates the energy output per cycle, which is determined by the output charges and the rectification voltage.

In practice, the implementation of FBR in triboelectric energy harvesting faces different challenges according to application scenarios. In low-power applications such as bio-energy harvesting, the input voltage is low (smaller than 5 V) so the rectifier should emphasize the suppression of the leakage current and conduction loss, while in high-power harvesting applications, it must tolerate high rectification voltage and extract as much energy as possible from TENG but voltage drop on the diode is comparatively negligible.

DYNAMIC-LEAKAGE-SUPPRESSION FBR

A dynamic-leakage-suppression FBR (DLS-FBR) is reported and employed to harvest kinetic energy from the human body, which is a typical low-power application scenario for triboelectric energy harvesting [1]. It is implemented with four cross-coupled CMOS pairs, each of which is composed of a PMOS and an NMOS gated by the source of each other. This configuration guarantees an off-voltage further from 0 and thus suppresses leakage current by more than 1000× at 0.6 V.

DUAL-OUTPUT RECTIFIER

Different from other transducers, TENG has a small time-varying internal capacitance, leading to an asymmetric and fast-changing output voltage. An integrated high-voltage dual-output rectifier (DOR) is reported to make full use of the asymmetric output of TENG [2]. It utilizes the high-voltage bipolar-CMOS-DMOS (BCD) technology, of which the double-diffused MOS (LDMOS) has a breakdown voltage of up to 70 V. A higher voltage can contribute to more energy extracted from TENG. The conventional FBR has a single output terminal, while in this work, it is split into two. The rectification voltages

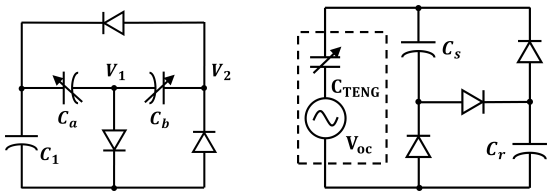

Figure 2.2: Bennet's charge doubler in (a) electrostatic voltage conditioning [6] and (b) triboelectric voltage conditioning [8].

at different output terminals are set differently to extract more energy. This also eliminates part of the phase difference. In the implementation, a high voltage protector is designed to avoid the current leakage between the outputs of DOR [2]. This architecture is improved by removing the protector and isolating the outputs with an inductor, and thus achieves suppression in the power dissipation [3], [4]. Additionally, maximum power point tracking (MPPT) technique is employed and implemented separately for either output terminal. In summary, DOR achieves better energy extraction performance than FBR, and is advantageous in passive conversion.

2.1.2. BENNET'S DOUBLER OF ELECTRICITY

Bennet's doubler of electricity was first proposed hundreds of years ago and was designed to induce and extract extra charge by shifting the capacitance at the beginning [5]. Its application in charging storage elements is illustrated in Fig. 2.2a [6]. For each working cycle, the variable capacitor C_a shrinks its capacitance first to decrease the voltage V_1 and induce charges on the other variable capacitor C_b. Then C_a resets while C_b decreases its capacitance to increase the voltage V_2 so that extra charges are pumped back to the storage element C_1. At the end of each cycle, the charge on C_1 increases, and so is the energy. This technique has been used in electrostatic energy harvesting as these variable capacitors are identical to the electrostatic pumps of electrostatic generator [7]. Since the internal capacitor of TENG is also variable, the implementation of Bennet's doubler in triboelectric energy harvesting is explored.

The first application of Bennet's doubler in triboelectric energy harvesting is proposed by [8] with the structure presented in Fig. 2.2b. To extract charge from TENG and decrease the output voltage at the meanwhile, this structure is different from the prior Bennet's doubler and utilizes two static capacitors C_s and C_r to halve the output voltage. In each cycle, C_s and C_r extract charges from TENG in series when its internal capacitance C_{TENG} is small, and transfer more charges back in parallel when C_{TENG} is large. There are two operation modes determined by the ratio between the maximum and the minimum of C_{TENG}, which is denoted as μ. When $\mu > 2$, Bennet's doubler works in the exponential mode that the output voltage diverges and increases exponentially. When $\mu < 2$, the voltage will increase convergently and saturate after a certain number of cycles [8]. Commonly, C_{TENG} varies significantly, so Bennet's doubler usually works in the exponential mode in triboelectric energy harvesting. In this case, the charge extracted

to C_s and C_r per cycle will increase exponentially, as well as the power output; hence the energy extracted by Bennet's doubler can easily exceed that of the passive full-bridge rectifier, where the charge output decreases when the rectification voltage increases. In addition, the energy gained by Bennet's doubler concentrates on the capacitor with the largest capacitance among C_{TENG}, C_s, and C_r, which makes it easy to be harvested [8].

Despite the advantages in extracting electrostatic energy, Bennet's Doubler has never been implemented on chip due to the high voltage. Additionally, Bennet's Doubler does not completely eliminate the power loss caused by the phase difference between voltage and current. If the passive diodes in this topology is replaced by synchronized active switch, the energy extraction performance is expected to be boosted.

2.2. ACTIVE CONVERTERS

Active converters are implemented with active switches that have lower conversion loss compared to passive devices. Though additional gate drivers and control circuit are required, some actively-switching converters can tackle the polarity difference between voltage and current outputs of TENG, which significantly increases the power output by multiple times that of standard energy harvesting circuit.

In this section, two synchronous switching techniques are introduced, named synchronous electric charge extraction (SECE) and synchronized-switch harvesting respectively. Both have been widely applied in piezoelectric energy harvesting to avoid the efficiency degradation caused by the polarity difference.

2.2.1. SYNCHRONOUS ELECTRIC CHARGE EXTRACTION (SECE)

SECE is a popular active rectification technique to boost energy extraction performance and was first designed for piezoelectric energy harvesting [9]. The typical circuit and voltage waveform is illustrated in Fig. 2.3a and Fig. 2.3b respectively. Different from the standard energy harvesting circuit, the rectifier is directly connected to the voltage regulator without a rectification capacitor. For most time in each semi-period, the transducer is isolated, so the output voltage is identical to the open-circuit voltage. When the voltage reaches an extremum, the inductor extracts the energy rapidly through the red path in phase 1 (ϕ_1), as presented in Fig. 2.3a. Since all charges accumulated on the internal capacitor are extracted, the voltage is reset at the end of ϕ_1, so there is no polarity difference between current and voltage output. Then the source is again isolated in the next semi-period when the energy temporarily stored in the inductor is transferred to the storage element C_{store} through the blue path in phase 2 (ϕ_2) [10]. In this way, the energy output is enhanced compared to the standard energy harvesting circuit because the charge is extracted and harvested at a higher voltage. Note that the quadra-switch design realizes a buck-boost regulator, so theoretically, the output of SECE can be directly used to power electronic devices.

The energy output of TENG enhanced by SECE is analyzed and presented by the V-Q plot in Fig. 2.3c. Due to the open-circuit phase in SECE, the charge is extracted from TENG at V_{OC} so the energy output is boosted. The shaded area presents the theoretical extra energy output in each cycle compared to the standard energy harvesting circuit, which is considerable and verified in discrete circuits [11], [12].

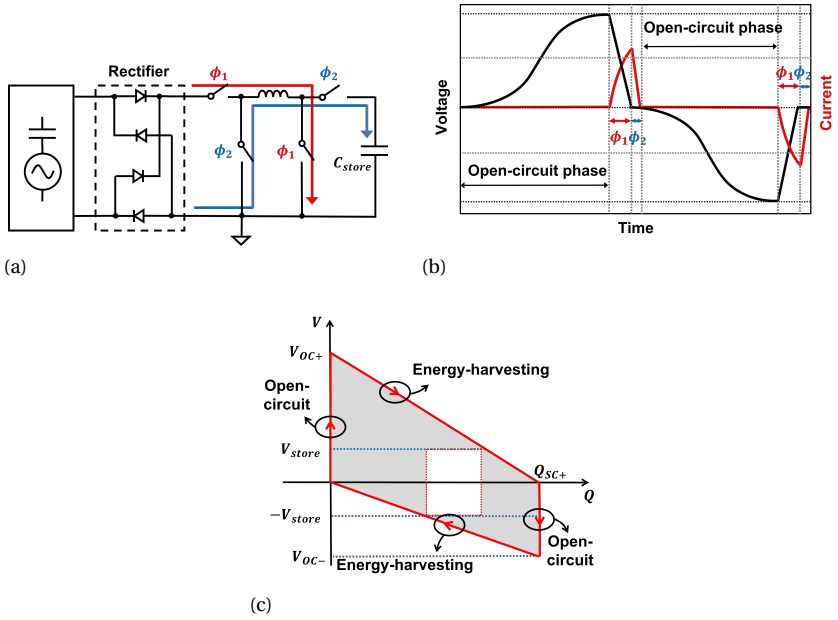

Figure 2.3: (a) Schematic of a SECE interface connected to TENG with (b) operation voltage and current waveform and (c) V-Q plot of TENG.

Due to the high open-circuit voltage of TENG, most implementations of SECE in extracting triboelectric energy are discrete circuits with mechanical switches. Some switches utilize the structure of TENG and turn on autonomously when the electrode moves to the extremum [13], [14]. However, this design requires the electrode to move regularly so it is incompatible in different scenarios. The current and voltage detector implemented by CMOS technology with high-voltage integrated interface can be helpful in the application of SECE in harvesting triboelectric energy. A multi-shot energy extraction technique implemented on-chip has been proposed recently, utilizing SECE in limited voltage tolerance [15].

2.2.2. SYNCHRONIZED-SWITCH HARVESTING

The synchronized-switch harvesting technique is specialized to eliminate the polarity difference between voltage and current outputs to extract more energy. Its simplest topology is composed of a full-bridge rectifier (FBR) and a switch placed across the energy source. The switch is turned on when the direction of the current shifts to remove the residual charge and reset the voltage. Thus it is named synchronous short-circuit rectifier (SSCR). It has been proven to be effective to synchronize the voltage and current when TENG moves to the extremum [16]. Besides, this synchronous short-circuit path was recently added to the SECE interface in piezoelectric energy harvesting to ensure stability and increase the harvestable energy bandwidth [17], [18].

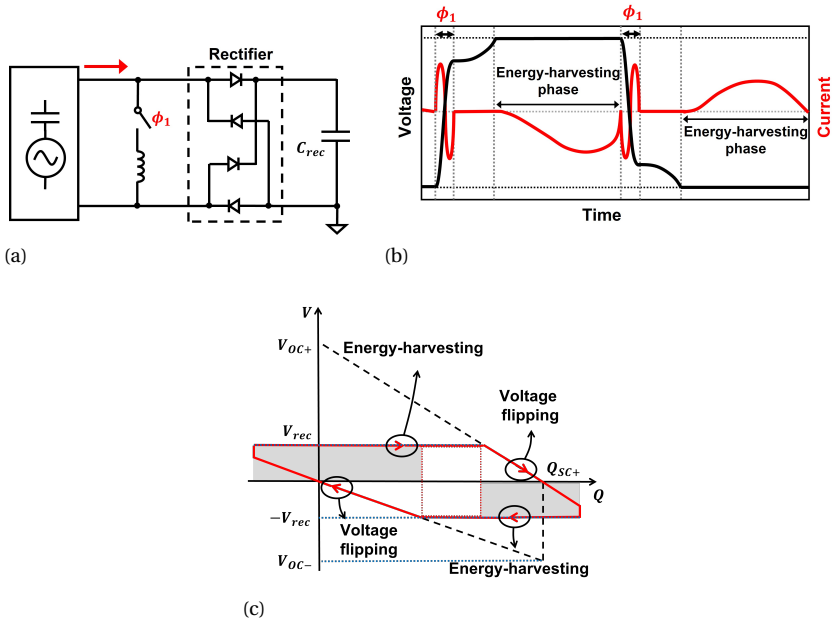

Figure 2.4: (a) Schematic of a parallel-SSHI interface connected to TENG with (b) operation voltage and current waveform and (c) V-Q plot of TENG.

However, a large part of the energy accumulated on the internal capacitor is wasted by SSCR in short-circuit phase. This can be improved by utilizing an inductor to flip the voltage instead of resetting it, which is the synchronized-switch harvesting on inductor (SSHI) technique i.e., bias-flipping rectifier. Based on different topologies of inductor connection, it can be divided into two types: parallel-SSHI and series-SSHI [19]. The typical parallel-SSHI circuit and operation waveform is illustrated in Fig. 2.4a and Fig. 2.4b respectively. When the current direction shifts, the switch will be turned on so the voltage of the source, which was equal to the rectification voltage, is flipped by the inductor [20]. When the current in the inductor is zero, the voltage-flipping phase ϕ_1 ends so the switch is turned off. Due to the nonideality of the inductor, the voltage across the internal capacitor cannot be completely flipped so it needs to be charged to the rectification voltage before the current is harvested. Nevertheless, parallel-SSHI saves much energy from discharging the internal capacitor of the source and contributes to efficiency boosting especially when the rectification voltage is high. Series-SSHI has two ways of implementation. The first one has a similar phenomenon to that of parallel-SSHI but flips voltage via the shorted bridge rectifier rather than an independent path [21]. The other kind of series-SSHI is closer to SECE, with the bridge rectifier cut-off for most of the time and the energy extracted at the same time as voltage flipping [22], [23].

SSHI rectifiers can also be implemented in triboelectric energy harvesting. The V-

Q plot of TENG with a parallel-SSHI interface is presented in Fig. 2.4c. The shadowed area in Fig. 2.4c is the extra energy harvested by the parallel-SSHI rectifier compared to the standard energy harvesting circuit. The parallel-SSHI is first implemented in triboelectric energy harvesting by [24] in a discrete circuit. Then the first integrated parallel-SSHI triboelectric energy harvesting circuit was implemented in [25] with an inductive step-down converter and a switched-capacitor DC-DC converter in series for voltage conditioning. In addition, thanks to the LDMOS, series-SSHI is more feasible since a short-circuit loop can be easily established within FBR. A double-stacked-chip series-SSHI employing an intrinsic fractal switched-capacitor converter (FSCC) is reported in [26], [27]. It boosts energy harvesting by doubling the voltage tolerance of the harvester via two series-connected FBRs and storage capacitors on two stacked chips. When the current output is 0, both FBRs will be shorted to flip the voltage across TENG. This active converter is driven by an external power source, which is also the storage element. Another series-SSHI triboelectric energy harvester is reported in [28].

Despite the advantages of the SSHI technique, it is not fully integrated due to the off-chip inductor. Inductor also brings other problems such as difficult control of flipping time and varying inductance, which lead to conversion loss [29], [30]. In this case, an inductor-less bias-flip rectifier was explored and implemented by the switched-capacitor technique, which is called synchronized switch harvesting on capacitors (SSHC) [31], [32]. To achieve higher efficiency, multiple capacitors are necessary to flip the voltage smoothly to reduce the charge-sharing loss, which can be implemented with more parallel stages [33] or phase-split configuration [32]. This SSHC converter can be fully integrated. However, considering the variable capacitance C_{TENG}, the conventional SSHC circuit achieves lower efficiency in triboelectric energy harvesting than in piezoelectric energy harvesting so it needs to be redesigned before being applied.

2.2.3. MAXIMUM POWER POINT TRACKING

The power output is proportional to the real-time product of the voltage and current output of the energy source. The condition under which the system has the maximum power output is defined as the maximum power point (MPP) as illustrated in Fig. 2.5a, and the technique to track and maintain the voltage at the maximum power point is named maximum power point tracking (MPPT) and it plays an important role in energy harvesting systems. If the energy extracted from the transducer is consumed directly by a load, the maximum power point is reached when the load impedance is equal to the internal impedance of the energy source [34]. Since the impedance of TENG is time-varying, an active impedance matching method was studied in [35] to track it with a negative impedance converter model. On the other hand, when the energy is to be harvested and stored, impedance matching is not feasible but the voltage across the storage element is to be controlled. For instance, in a standard energy harvesting circuit, the maximal power output is tracked by monitoring the rectification voltage on the storage element since the charge output in one cycle is normally relative to the rectification voltage.

There are several methods to implement MPPT, including perturb and observe (P&O), incremental conductance (IncCond), and fractional open-circuit voltage (FOCV). Both P&O and IncCond track the maximum power point continuously by adjusting the recti-

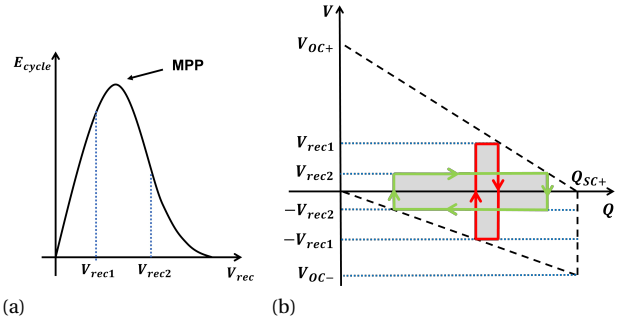

Figure 2.5: (a) Typical pattern of output energy per cycle versus rectification voltage. (b) V-Q plot of MPPT in triboelectric energy harvesting.

fication voltage and then monitoring the difference in power output i.e., the change of energy stored in the load capacitor [36]. These two techniques are accurate but complicated to implement. On the other hand, the FOCV methodology is much simpler to be implemented. For many transducers including piezoelectric transducers, electrostatic transducers, and triboelectric nanogenerators (TENG), the maximal power output usually occurs around a certain voltage which has a fixed ratio to the open-circuit voltage [37]. Indeed, the V-Q plot that reflects the energy output of each cycle can contribute to virtually seeking the maximum power point of TENG as presented in Fig. 2.5b. The red and green rectangles indicate the standard energy harvesting circuit working at different rectification voltages V_{rec1} and V_{rec2} respectively, while their areas represent the corresponding energy output. MPPT technique should track the rectification voltage when the energy output reaches the maximum i.e., the maximum rectangle enclosed by the dashed lines. When the properties of TENG are fixed, the maximum power point can be easily figured out mathematically, which is

$$V_{rec,mppt} = \frac{1}{2}\frac{V_{OC-}V_{OC+}}{V_{OC-} + V_{OC+}} \tag{2.1}$$

where V_{OC-} and V_{OC+} represent the asymmetric open-circuit voltage of TENG. By monitoring these two voltages and maintaining the rectification voltage at the $V_{rec,mppt}$, MPPT can be implemented with less energy loss and a simpler control system. Due to its simplicity in implementation and relatively-high accuracy, the FOCV technique is widely implemented in kinetic energy harvesting.

MPPT technique can also be utilized to maintain the maximal power output in active converters, where impedance matching and storage voltage optimization are also required [38]. So far, it has not been integrated into active triboelectric energy harvesting. In both SECE and SSHI interface, the maximum power point is determined by two parameters: the maximal open-circuit voltage of TENG and the nonideality of the inductor [39]. Both parameters may vary in practice, which makes it difficult to track the maximal power output. Besides, the rectification voltage at the maximum power point can be multiple times the open-circuit voltage of TENG, which can hardly be measured

by integrated circuit [40]. A duty-cycle-based MPPT for triboelectric energy harvesting is proposed and implemented in this thesis to tackle this problem.

2.3. COMPARISON AND DISCUSSION

The state-of-the-arts of the triboelectric energy converters in the previous 5 years are summarized in Table 2.1. This table summarizes their process, conversion techniques and performance and evaluates the circuit complexity and figure-of-merit (FoM). In triboelectric energy harvesting, the FoM is defined as the energy extracted from TENG per cycle with a normalized size. It is derived from the following equation:

$$FoM = \frac{P_{EXT}}{f_{OP} \times S} \tag{2.2}$$

where P_{EXT} represents the power extracted from TENG i.e., the power input to the harvester, and f_{OP} represents the operational frequency. It depicts the absolute energy extraction capacity of the harvester while the fraction of P_{EXT} over the power extracted by FBR (P_{FBR}) only reflects the relative energy extraction capability. Therefore, a higher FoM corresponds to higher energy extraction capacity of harvester and better transduction performance of TENG. Besides, the voltage regulator employed in each work is mentioned, as well as the relevant results such as power conversion efficiency (PCE) and output voltage.

Among the state-of-the-arts, contact-separation TENG (CS TENG) is the most employed TENG due to easier fabrication and modeling. Wind TENG is also reported to be employed in harvester development. Different from the aforementioned fundamental TENG, it has a fixed internal capacitance and works at a higher operational frequency which is identical to the vibration of triboelectric film driven by the airflow, so the energy extraction from it is relatively easier [27], [28]. In addition, one case of piezoelectric energy harvesting is included to present the difference between energy extraction from TENG and piezoelectric transducer (PT).

In general, the harvesters implemented with passive devices such as FBR and Bennet's Doubler are simpler than those with active switches, but they have bad adaptivity and compatibility without voltage regulation implemented by active switches. IC technology is advantageous in implementing active converters in miniaturization and lower leakage but is limited in voltage tolerance. That is the reason why Bennet's Doubler implemented discretely has higher extraction capacity than integrated FBR, dual-output rectifier (DOR), synchronized-switch harvesting on inductor (SSHI) and synchronous charge extraction (SCE) based on the FoM. Among the IC works implemented with 65-nm CMOS or 0.18-um BCD process, their extraction voltage V_{EXT} are lower than 70 V due to process limitation and thus achieves relatively lower FoM, except the work [27] which exceeds the voltage limitation via the multi-chip-stacked bias-flip (MCS-BF) technique. As a consequence, its FoM is more than 4 times higher than other IC works.

Table 2.1: COMPARISON TABLE OF THE STATE-OF-THE-ART

Rectifier	Passive converters					Active converters				
	FBR			Bennet's doubler		SECE	P-SSHI	S-SSHI		SSHCI
Reference	[41]	[2]	[4]	[8]	[42]	[15]*	[25]	[27]	[28]	[43]
Transducer	CS TENG	CS TENG	CS TENG	CS TENG	CS TENG	CS TENG	CS TENG	Wind TENG	Wind TENG	PT
Process	65 nm CMOS	0.18 um BCD	0.18 um BCD	Discrete	Discrete	0.18 um BCD	0.18 um BCD	0.18 um BCD	0.18 um BCD	0.18 um BCD
Modification	-	Dual-output rectifier	Dual-output rectifier	-	-	Multi-shot SCE	-	MCS-BF	-	-
Regulation	SCC	Dual-input BUCK	Dual-input BUCK	-	BUCK	BUCK-BOOST	BUCK +SCC	SCC	SCC	BUCK
MPPT	-	FOCV	FOCV	-	-	-	-	-	-	FOCV
$V_{EXT}(V)$	2.5	3.5 - 70	<70	835	450*	<70	12-70	$65 \times N$	<65	<5
PCE	88%	52.9%	75.6%	-	31.60%	63.28%	32.7%	70.7%	79.3%	83%
Output voltage	1.2	2 - 5	2.8 - 3.3	-	17	2 - 20	2	3.1 - 4.3	2.7 - 4.2	1.6 - 4.6*
$P_{EXT}(\mu W)$	2.4 - 15.6	4.5 - 20.9	3.9 - 10.5	70*	152	90.3	2.95	1200	300	29.2
FoM (nJ/cm^2)	-	80	64	140*	840	-	44	380	95	20
P_{EXT}/P_{FBR}	-	-	-	21×	7.7×	1.91×	1.62×	3.14×	-	5.44×

* Simulated results. ** Estimated.

Among the IC triboelectric harvesters, those employing bias-flip techniques have better energy extraction performance than passive rectifiers so it is necessary for high-power energy harvesting. Furthermore, it is noted that few works in triboelectric energy harvesting employ MPPT. The reason is that FOCV is not suitable for triboelectric energy harvesting due to the small internal impedance and high open-circuit voltage of TENG, while the P&O is difficult to implement.

BIBLIOGRAPHY

[1] J. S. Y. Tan, J. H. Park, J. Li, *et al.*, "A fully energy-autonomous temperature-to-time converter powered by a triboelectric energy harvester for biomedical applications," *IEEE Journal of Solid-State Circuits*, vol. 56, no. 10, pp. 2913–2923, 2021, ISSN: 1558-173X. DOI: 10.1109/JSSC.2021.3080383.

[2] I. Park, J. Maeng, M. Shim, J. Jeong, and C. Kim, "A high-voltage dual-input buck converter achieving 52.9% maximum end-to-end efficiency for triboelectric energy-harvesting applications," *IEEE Journal of Solid-State Circuits*, vol. 55, no. 5, pp. 1324–1336, 2020, ISSN: 1558-173X. DOI: 10.1109/JSSC.2019.2942370.

[3] I. Park, J. Maeng, M. Shim, J. Jeong, and C. Kim, "A bidirectional high-voltage dual-input buck converter for triboelectric energy-harvesting interface achieving 70.72% end-to-end efficiency," in *2019 Symposium on VLSI Circuits*, IEEE, 2019, pp. C326–C327, ISBN: 4863487207.

[4] J. Maeng, I. Park, M. Shim, J. Jeong, and C. Kim, "A high-voltage dual-input buck converter with bidirectional inductor current for triboelectric energy-harvesting applications," *IEEE Journal of Solid-State Circuits*, vol. 56, no. 2, pp. 541–553, 2021, ISSN: 1558-173X. DOI: 10.1109/JSSC.2020.3012991.

[5] A. C. M. de Queiroz, "Electrostatic vibrational energy harvesting using a variation of bennet's doubler," in *2010 53rd IEEE International Midwest Symposium on Circuits and Systems*, 2010, pp. 404–407. DOI: 10.1109/MWSCAS.2010.5548752.

[6] A. C. M. d. Queiroz and M. Domingues, "The doubler of electricity used as battery charger," *IEEE Transactions on Circuits and Systems II: Express Briefs*, vol. 58, no. 12, pp. 797–801, 2011, ISSN: 1558-3791. DOI: 10.1109/TCSII.2011.2173963.

[7] V. P. Dragunov, D. I. Ostertak, and R. E. Sinitskiy, "New modifications of a bennet doubler circuit-based electrostatic vibrational energy harvester," *Sensors and Actuators A: Physical*, vol. 302, p. 111 812, 2020, ISSN: 0924-4247. DOI: https://doi.org/10.1016/j.sna.2019.111812. [Online]. Available: https://www.sciencedirect.com/science/article/pii/S0924424719314402.

[8] A. Ghaffarinejad, J. Y. Hasani, R. Hinchet, *et al.*, "A conditioning circuit with exponential enhancement of output energy for triboelectric nanogenerator," *Nano Energy*, vol. 51, pp. 173–184, 2018, ISSN: 2211-2855.

[9] E. Lefeuvre, A. Badel, C. Richard, and D. Guyomar, "Piezoelectric energy harvesting device optimization by synchronous electric charge extraction," *Journal of Intelligent Material Systems and Structures*, vol. 16, no. 10, pp. 865–876, 2005, ISSN: 1045-389X. DOI: 10.1177/1045389X05056859. [Online]. Available: https://doi.org/10.1177/1045389X05056859.

[10] A. Morel, A. Quelen, P. Gasnier, *et al.*, "A shock-optimized sece integrated circuit," *IEEE Journal of Solid-State Circuits*, vol. 53, no. 12, pp. 3420–3433, 2018, ISSN: 1558-173X. DOI: 10.1109/JSSC.2018.2868299.

[11] X. Cheng, L. Miao, Y. Song, *et al.*, "High efficiency power management and charge boosting strategy for a triboelectric nanogenerator," *Nano Energy*, vol. 38, pp. 438–446, 2017, ISSN: 2211-2855.

[12] F. Xi, Y. Pang, W. Li, *et al.*, "Universal power management strategy for triboelectric nanogenerator," *Nano Energy*, vol. 37, pp. 168–176, 2017, ISSN: 2211-2855.

[13] H. Qin, G. Cheng, Y. Zi, *et al.*, "High energy storage efficiency triboelectric nanogenerators with unidirectional switches and passive power management circuits," *Advanced Functional Materials*, vol. 28, no. 51, p. 1 805 216, 2018, ISSN: 1616-301X. DOI: https://doi.org/10.1002/adfm.201805216. [Online]. Available: https://doi.org/10.1002/adfm.201805216.

[14] J. Yang, F. Yang, L. Zhao, *et al.*, "Managing and optimizing the output performances of a triboelectric nanogenerator by a self-powered electrostatic vibrator switch," *Nano Energy*, vol. 46, pp. 220–228, 2018, ISSN: 2211-2855. DOI: https://doi.org/10.1016/j.nanoen.2018.02.013. [Online]. Available: https://www.sciencedirect.com/science/article/pii/S2211285518300740.

[15] M. Pathak, S. Xie, C. Huang, and R. Kumar, "High-voltage triboelectric energy harvesting using multi-shot energy extraction in 70-v bcd process," *IEEE Transactions on Circuits and Systems II: Express Briefs*, vol. 69, no. 5, pp. 2513–2517, 2022, ISSN: 1558-3791. DOI: 10.1109/TCSII.2022.3160676.

[16] Y. Zi, J. Wang, S. Wang, *et al.*, "Effective energy storage from a triboelectric nanogenerator," *Nature communications*, vol. 7, no. 1, pp. 1–8, 2016, ISSN: 2041-1723.

[17] A. Morel, P. Gasnier, Y. Wanderoild, G. Pillonnet, and A. Badel, "Short circuit synchronous electric charge extraction (sc-sece) strategy for wideband vibration energy harvesting," in *2018 IEEE International Symposium on Circuits and Systems (ISCAS)*, 2018, pp. 1–5, ISBN: 2379-447X. DOI: 10.1109/ISCAS.2018.8351559.

[18] A. Morel, A. Quelen, C. A. Berlitz, *et al.*, "Fast-convergence self-adjusting sece circuit with tunable short-circuit duration exhibiting 368% bandwidth improvement," *IEEE Solid-State Circuits Letters*, vol. 3, pp. 222–225, 2020, ISSN: 2573-9603. DOI: 10.1109/LSSC.2020.3012340.

[19] I. C. Lien, Y. C. Shu, W. J. Wu, S. M. Shiu, and H. C. Lin, "Revisit of series-sshi with comparisons to other interfacing circuits in piezoelectric energy harvesting," *Smart Materials and Structures*, vol. 19, no. 12, p. 125 009, 2010, ISSN: 0964-1726 1361-665X. DOI: 10.1088/0964-1726/19/12/125009. [Online]. Available: http://dx.doi.org/10.1088/0964-1726/19/12/125009.

[20] D. A. Sanchez, J. Leicht, F. Hagedorn, E. Jodka, E. Fazel, and Y. Manoli, "A parallel-sshi rectifier for piezoelectric energy harvesting of periodic and shock excitations," *IEEE Journal of Solid-State Circuits*, vol. 51, no. 12, pp. 2867–2879, 2016, ISSN: 1558-173X. DOI: 10.1109/JSSC.2016.2615008.

[21] L. Wu and D. S. Ha, "A self-powered piezoelectric energy harvesting circuit with an optimal flipping time sshi and maximum power point tracking," *IEEE Transactions on Circuits and Systems II: Express Briefs*, vol. 66, no. 10, pp. 1758–1762, 2019, ISSN: 1558-3791. DOI: 10.1109/TCSII.2019.2924963.

[22] S. Fang, H. Xia, Y. Xia, *et al.*, "An efficient piezoelectric energy harvesting circuit with series-sshi rectifier and fnov-mppt control technique," *IEEE Transactions on Industrial Electronics*, vol. 68, no. 8, pp. 7146–7155, 2021, ISSN: 1557-9948. DOI: 10.1109/TIE.2020.3007054.

[23] H. Xia, Y. Xia, G. Shi, *et al.*, "A self-powered s-sshi and sece hybrid rectifier for pe energy harvesters: Analysis and experiment," *IEEE Transactions on Power Electronics*, vol. 36, no. 2, pp. 1680–1692, 2021, ISSN: 1941-0107. DOI: 10.1109/TPEL.2020.3007694.

[24] X. Li and Y. Sun, "An sshi rectifier for triboelectric energy harvesting," *IEEE Transactions on Power Electronics*, vol. 35, no. 4, pp. 3663–3678, 2020, ISSN: 0885-8993.

[25] I. Kara, M. Becermis, M. A. A. Kamar, M. Aktan, H. Dogan, and S. Mutlu, "A 70-to-2 v triboelectric energy harvesting system utilizing parallel-sshi rectifier and dc-dc converters," *IEEE Transactions on Circuits and Systems I: Regular Papers*, vol. 68, no. 1, pp. 210–223, 2021, ISSN: 1558-0806. DOI: 10.1109/TCSI.2020.3025468.

[26] L. Jiho, L. Sang-Han, K. Gyeong-Gu, K. Jae-Hyun, C. Gyu-Hyeong, and K. Hyun-Sik, "A 130v triboelectric energy-harvesting interface in 0.18um bcd with scalable multi-chip-stacked bias-flip and daisy-chained synchronous signaling technique," in *2018 IEEE International Solid-State Circuits Conference - (ISSCC)*, 2022.

[27] J. Lee, S. H. Lee, G. G. Kang, J. H. Kim, G. H. Cho, and H. S. Kim, "A triboelectric energy-harvesting interface with scalable multi-chip-stacked bias-flip and daisy-chained synchronous signaling techniques," *IEEE Journal of Solid-State Circuits*, pp. 1–15, 2022, ISSN: 1558-173X. DOI: 10.1109/JSSC.2022.3193738.

[28] S. H. Lee, Y. W. Jeong, S. J. Park, and S. U. Shin, "A rectifier-reusing bias-flip energy harvesting interface circuit with adaptively reconfigurable sc converter for wind-driven triboelectric nanogenerator," *IEEE Transactions on Industrial Electronics*, pp. 1–10, 2022, ISSN: 1557-9948. DOI: 10.1109/TIE.2022.3220848.

[29] S. Javvaji, V. Singhal, V. Menezes, R. Chauhan, and S. Pavan, "Analysis and design of a multi-step bias-flip rectifier for piezoelectric energy harvesting," *IEEE Journal of Solid-State Circuits*, vol. 54, no. 9, pp. 2590–2600, 2019, ISSN: 1558-173X. DOI: 10.1109/JSSC.2019.2917158.

[30] Z. Chen, M.-K. Law, P.-I. Mak, W.-H. Ki, and R. P. Martins, "22.2 a 1.7mm2 inductorless fully integrated flipping-capacitor rectifier (fcr) for piezoelectric energy harvesting with 483% power-extraction enhancement," in *2017 IEEE International Solid-State Circuits Conference (ISSCC)*, 2017, pp. 372–373. DOI: 10.1109/ISSCC.2017.7870416.

[31] S. Du and A. A. Seshia, "An inductorless bias-flip rectifier for piezoelectric energy harvesting," *IEEE Journal of Solid-State Circuits*, vol. 52, no. 10, pp. 2746–2757, 2017, ISSN: 1558-173X. DOI: 10.1109/JSSC.2017.2725959.

[32] Z. Chen, M.-K. Law, P.-I. Mak, W.-H. Ki, and R. P. Martins, "Piezoelectric energy-harvesting interface using split-phase flipping-capacitor rectifier with capacitor reuse for input power adaptation," *IEEE Journal of Solid-State Circuits*, pp. 1–1, 2020, ISSN: 1558-173X. DOI: 10.1109/JSSC.2020.2989873.

[33] X. Yue and S. Du, "Voltage flip efficiency optimization of sshc rectifiers for piezoelectric energy harvesting," in *2021 IEEE International Symposium on Circuits and Systems (ISCAS)*, pp. 1–5, ISBN: 2158-1525. DOI: 10.1109/ISCAS51556.2021.9401330.

[34] S. Zargari, A. Rezania, Z. D. Koozehkanani, H. Veladi, J. Sobhi, and L. Rosendahl, "Effect of the inherent capacitance optimization on the output performance of triboelectric nanogenerators," *Nano Energy*, vol. 92, p. 106 740, 2022, ISSN: 2211-2855. DOI: https://doi.org/10.1016/j.nanoen.2021.106740. [Online]. Available: https://www.sciencedirect.com/science/article/pii/S2211285521009

[35] A. M. El-Mohandes and R. Zheng, "Active matching circuit to enhance the generated power of triboelectric nanogenerators," *Nano Energy*, vol. 80, p. 105 588, 2021, ISSN: 2211-2855.

[36] L. Costanzo, A. L. Schiavo, and M. Vitelli, "Active interface for piezoelectric harvesters based on multi-variable maximum power point tracking," *IEEE Transactions on Circuits and Systems I: Regular Papers*, vol. 67, no. 7, pp. 2503–2515, 2020, ISSN: 1558-0806. DOI: 10.1109/TCSI.2020.2977495.

[37] M. Shim, J. Kim, J. Jeong, S. Park, and C. Kim, "Self-powered 30w to 10 mw piezoelectric energy harvesting system with 9.09 ms/v maximum power point tracking time," *IEEE Journal of Solid-State Circuits*, vol. 50, no. 10, pp. 2367–2379, 2015, ISSN: 0018-9200. DOI: 10.1109/JSSC.2015.2456880.

[38] M. Dini, A. Romani, M. Filippi, V. Bottarel, G. Ricotti, and M. Tartagni, "A nanocurrent power management ic for multiple heterogeneous energy harvesting sources," *IEEE Transactions on Power Electronics*, vol. 30, no. 10, pp. 5665–5680, 2015, ISSN: 0885-8993. DOI: 10.1109/TPEL.2014.2379622.

[39] M. Pathak and R. Kumar, "Synchronous inductor switched energy extraction circuits for triboelectric nanogenerator," *IEEE Access*, vol. 9, pp. 76 938–76 954, 2021, ISSN: 2169-3536.

[40] S. Li, A. Roy, and B. H. Calhoun, "A piezoelectric energy-harvesting system with parallel-sshi rectifier and integrated maximum-power-point tracking," *IEEE Solid-State Circuits Letters*, vol. 2, no. 12, pp. 301–304, 2019, ISSN: 2573-9603. DOI: 10.1109/LSSC.2019.2951394.

[41] K. Rawy, R. Sharma, H. J. Yoon, U. Khan, S. W. Kim, and T. T. Kim, "An 88% efficiency 2.4uw to 15.6uw triboelectric nanogenerator energy harvesting system based on a single-comparator control algorithm," in *2018 IEEE Asian Solid-State Circuits Conference (A-SSCC)*, 2018, pp. 33–36. DOI: 10.1109/ASSCC.2018.8579338.

[42] H. Zhang, D. Galayko, and P. Basset, "A conditioning system for high-voltage electrostatic/triboelectric energy harvesters using bennet doubler and self-actuated hysteresis switch," in *2019 20th International Conference on Solid-State Sensors, Actuators and Microsystems Eurosensors XXXIII (TRANSDUCERS EUROSENSORS XXXIII)*, 2019, pp. 346–349. DOI: 10.1109/TRANSDUCERS.2019.8808359.

[43] B. Çiftci, S. Chamanian, A. Koyuncuoğlu, A. Muhtaroğlu, and H. Külah, "A low-profile autonomous interface circuit for piezoelectric micro-power generators," *IEEE Transactions on Circuits and Systems I: Regular Papers*, vol. 68, no. 4, pp. 1458–1471, 2021, ISSN: 1558-0806. DOI: 10.1109/TCSI.2021.3053503.

3

THE PROPOSED HARVESTER FOR TRIBOELECTRIC ENERGY HARVESTING

To improve the energy extraction efficiency from TENG, the bias-flip technique is necessary to eliminate the phase difference between the output current and voltage. Compared to SSHI, SSHC has a smaller form factor. Besides, due to the small internal capacitance of TENG, SSHC is advantageous since its flip efficiency can be maintained with a small flip capacitance, which makes it cost-efficient to be implemented on the chip. Therefore, a 70-V SSHC rectifier with duty-cycle-based MPPT is proposed in this thesis. Different from the conventional SSHC rectifier, two separated SSHC rectifiers are utilized in this work to handle the asymmetric characteristics of TENG. Furthermore, to tackle the difficulty in tracking the MPP of TENG, the relationship between the conducting duty cycle of the rectifier and the extracted power is explored. By detecting the conducting duty cycle of the rectifier, the MPP voltage can be tracked without measuring the open-circuit voltage of TENG.

In the rest sections of this chapter, the proposed Dual-SSHC (D-SSHC) rectifier and the duty-cycle-based MPPT (DCB-MPPT) will be introduced in turn. Then the implementation details will be elaborated.

3.1. DUAL-SSHC RECTIFIER

3.1.1. OPERATIONAL PRINCIPLE

TENG outputs asymmetric voltage in different phases. As presented in Fig. 1.4, in the positive phase (ϕ_+), current flows in the positive direction, and the C_{TE} is suppressed; thus the voltage across it is boosted until the voltage magnitude reaches the rectification voltage V_{rec} at the output of the full-bridge rectifier (FBR). Note that the forward voltage on the diode of FBR is typically much smaller than V_{rec} in TEH, so it is negligible. Therefore, when the phase shifts from the ϕ_+ to the negative phase (ϕ_-), the voltage on C_{TE}

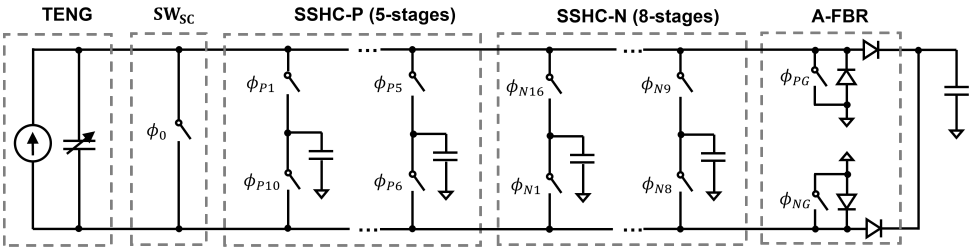

Figure 3.1: The proposed D-SSHC technique.

before flipping shall be equal to the V_{rec}. Then, C_{TE} increases during the ϕ_-. Despite the charge from I_{SC}, the magnitude of the voltage on C_{TE} is still lower than that in ϕ_+. For some TENGs, the voltage magnitude cannot reach the V_{rec} at the end of ϕ_-, thus the voltage to be flipped is different from the prior one. In this situation, energy is wasted to compensate for the flip voltage difference if only one SSHC is employed. The solution is given by the dual synchronized-switch harvesting on capacitor (D-SSHC) interface.

Fig. 3.1 presents the diagram of the proposed D-SSHC. In this interface, two SSHC blocks, SSHC-P and SSHC-N, are employed for voltage flipping when phase shifts from ϕ_+ to ϕ_- and from ϕ_- to ϕ_+ respectively. Since they operate separately, the waste of energy caused by the flip voltage difference is eliminated. Different from the conventional SSHC, the switched capacitors (SCs) in D-SSHC are not floated but have one side permanently grounded. This architecture can decrease the number of high-voltage switches (HVS) and parasitic capacitance in the circuit. To build the current loop when flipping, an active FBR (A-FBR) is proposed, utilizing the pair of n-type LDMOSs (laterally-diffused MOSFET) to ground one side of TENG. The operational control waveform of D-SSHC is presented in Fig. 3.2. At the start of ϕ_-, the SSHC-P operates to flip the voltage on the C_{TE}. The SCs work in the sequence $\phi_{P1} \rightarrow \phi_{P2} \rightarrow \phi_{P3} \rightarrow \phi_{P4} \rightarrow \phi_{P5} \rightarrow \phi_0 \rightarrow \phi_{P6} \rightarrow \phi_{P7} \rightarrow \phi_{P8} \rightarrow \phi_{P9} \rightarrow \phi_{P10}$. In this process, the low-voltage side of TENG is grounded, except during the ϕ_0 when the short-circuit switch (SW_S) works. When C_{TE} is shorted, it is not grounded but floated to save part of the charge [1]. While at the beginning of ϕ_+, the SSHC-N is activated, with the SCs operating in the following sequences $\phi_{N1} \rightarrow \phi_{N2} \rightarrow \phi_{N3} \rightarrow \phi_{N4} \rightarrow \phi_{N5} \rightarrow \phi_{N6} \rightarrow \phi_{N7} \rightarrow \phi_{N8} \rightarrow \phi_0 \rightarrow \phi_{N9} \rightarrow \phi_{N10} \rightarrow \phi_{N11} \rightarrow \phi_{N12} \rightarrow \phi_{N13} \rightarrow \phi_{N14} \rightarrow \phi_{N15} \rightarrow \phi_{N16}$. The grounding principle is the same as when SSHC-P operates.

3.1.2. PERFORMANCE ANALYSIS

The energy harvesting performance of the D-SSHC is mainly influenced by the flip efficiency and the flip delay. To quantize these factors, the parameters of the TENG model utilized in the simulation are presented in the Table.1.1 in section 1.3.

The flip efficiency (η_f) of SSHC is defined as the ratio of the voltage magnitude after flip over that before the flip and determined by the number of SCs and their capacitance [2]. Since the whole system is integrated on the chip, the total capacitance of all SCs is limited. When the capacitance of each switched capacitor in either SSHC is equal, η_f can be calculated by the following equation [3]:

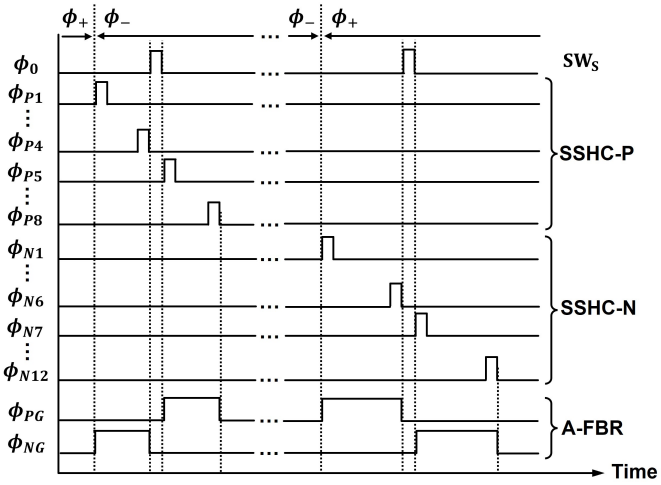

Figure 3.2: The synchronized control waveform of D-SSHC.

$$\eta_f = \frac{C_{Total}}{C_{Total} + C_S + C_{TE}}; \tag{3.1}$$

where C_{Total} represents the total capacitance of SCs and C_S represents the capacitance of each switched capacitor. When V_{rec} is high and nearly constant in one cycle, the output energy per cycle (E_c) can be calculated with the following equation:

$$E_c = C_{TE,min} V_{rec}(k_1 V_{OC,max} - k_2 V_{rec}); \tag{3.2}$$

$$k_1 = 1 + \eta_{f,np}; \quad k_2 = 1 - \eta_{f,np}\eta_{f,pn}; \tag{3.3}$$

where $C_{TE,min}$ represents the minimal C_{TE} and $V_{OC,max}$ represents the maximal open-circuit voltage of TENG. It can be observed that the flip efficiency when TENG shifts from ϕ_+ to ϕ_- ($\eta_{f,pn}$) and when TENG shifts from ϕ_- to ϕ_+ ($\eta_{f,np}$) have different contribution weights to E_c. In comparison, $\eta_{f,np}$ is more significant since $V_{OC,max}$ is typically multiple times of V_{rec}. Given that the C_{Total} in SSHC-N is 800pF and $C_{TE,max}$ is 100 pF, the theoretical $\eta_{f,np}$ versus different number of SCs is presented in Table. 3.1. To assure that $\eta_{f,np}$ is higher than 75%, SSHC-N is determined to contain 8 stages. Noted that the simulated flip efficiency is generally lower than the theoretical one, especially when more stages are applied. This is caused by the charge loss in SSHC due to the parasitic capacitance of LDMOS.

Regarding the $\eta_{f,pn}$, thanks to the small capacitance of $C_{TE,min}$ ($10\,pF$), it can be maintained higher than 70% with little capacitance and few stages theoretically. Therefore, the C_{Total} for SSHC-P is 200 pF, split into 5 stages.

The flip delay denotes the delay time between the zero-crossing time of the current and the start time of flip. According to the Fig. 1.4, I_{SC} increases significantly after the

Table 3.1: The flip efficiency for different numbers of SCs in SSHC-N.

The number of SCs in SSHC-N	flip efficiency $\eta_{f,np}$
1	45.5%
2	58.8%
3	65.2%
4	69.0%
5	71.4%
6	73.2%
7	74.5%
8	75.5%

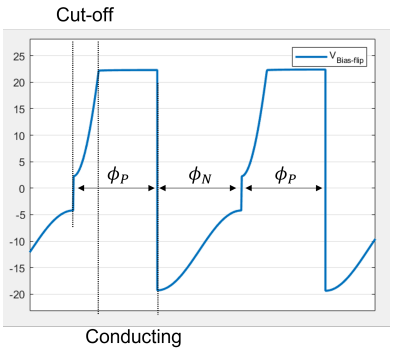

Figure 3.3: Example waveform of TENG conditioned by the bias-flip interface.

zero-crossing time when TENG shifts from ϕ_- to ϕ_+, while C_{TE} suppresses at the meantime. This weakens the voltage response and slows the zero-crossing detection. According to the simulation, the power degrades for approximately 10% and 25% when the flip delay is 2% and 4% of the operation period of TENG respectively, thus the zero-crossing detection needs to be fast.

3.2. DUTY-CYCLE-BASED MPPT

Energy loss occurs in a voltage flip, thus the voltage magnitude after the flip is lower than that before the flip as presented in Fig. 3.3. Before the energy-harvesting phase, the rectifier is cut-off. When the flip efficiency is higher, the voltage after flipping is higher and closer to the rectification voltage so that the cut-off duty cycle is lower. The cut-off duty cycle is defined as the ratio of the cut-off time over half of the period. For the bias-flip interface implemented in piezoelectric energy harvesting, the MPP voltage is concerned with the flip efficiency. This indicates a potential relationship between the flip efficiency and the cut-off duty cycle.

Based on the work of my supervisor Xinling, in bias-flip piezoelectric energy harvest-

ing, the MPP is reached when the cut-off duty cycle is 50%, which means the conducting time is equal to the cut-off time in one period. Inspired by this work, the corresponding relationship in triboelectric energy harvesting is explored. Due to the asymmetric capacitance of TENG in different phases, the MPP cannot be reached if current flows through the rectifier in ϕ_- [4]. Thus only the cut-off duty cycle in ϕ_+ needs to be considered. Based on the calculation attached in the appendix, the relationship between the cut-off duty cycle and the flip efficiency is:

$$D_{CO} = \frac{1}{2\pi}\arccos\frac{-\eta_{f,pn}\eta_{f,np}}{2-\eta_{f,pn}\eta_{f,np}}; \tag{3.4}$$

This equation is validated with simulation in Cadence with a precision higher than 90%. The imprecision is caused by approximation in the calculation that the thickness of the triboelectric film is negligible compared to the distance between electrodes when TENG reaches the MPP. To pursue precise cut-off duty cycle at MPP, the calculation would be too complicated. Actually, the small imprecision in duty cycle would not lead to serious MPPT efficiency degradation according to the simulation. Since the DCB-MPPT does not need to detect the high open-circuit voltage and has a good tracking efficiency, it is utilized in this work.

In practice, we need to detect the real cut-off duty cycle and compare it to the MPP cut-off duty cycle. If the real one exceeds that of the MPP one, it is indicated that the harvesting goes beyond the MPP and the rectification voltage needs to be decreased. We utilize a digital way to detect and record the cut-off time, with a voltage-controlled oscillator (VCO) and a counter. The operation period of TENG will be measured and counted first, then the MPP cut-off time is depicted. By measuring the cut-off time in the next cycle, the MPP state is detected.

Theoretically, the flip efficiency of an SSHC rectifier can be determined if knowing the internal capacitance of the transducer, flip capacitance, and the number of flip stages. However, in practice, the parasitic capacitance in the circuit influence the MPP cut-off duty cycle, thus a calibration in the duty cycle is necessary. When the product of $\eta_{f,pn}$ and $\eta_{f,np}$ increases from 0.2 to 0.6, the MPP cut-off duty cycle raises from around 54% to 64% as presented in Fig. 3.4. Thus, in practice, we first count the half of the ϕ_+, then add the calibration number to it. The summation is the MPP cut-off time we want.

3.3. IMPLEMENTATION

3.3.1. SYSTEM ARCHITECTURE AND WORKFLOW

The architecture of the whole system is presented in Fig. 3.5. The harvester is integrated on the chip except the power capacitors and the inductor. TENG is directly connected to the D-SSHC, including SSHC-P and SSHC-N, and an active FBR (A-FBR). The A-FBR integrates the function of FBR and zero-current detector (ZCD) to detect if the FBR is conducting or cut off. Once the harvester exceeds the MPP state, the DC-DC buck converter works to maintain the MPP and convert energy from the high voltage to a low one on C_{out}.

The conducting detection result is sent to the control system, whose workflow is presented in Fig. 3.6. When the current flowing in A-FBR drops to zero, SSHC-P starts to

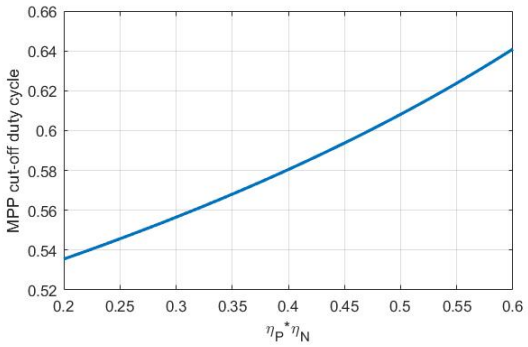

Figure 3.4: MPP cut-off duty cycle versus product of efficiencies, $\eta_{f,pn}$ and $\eta_{f,np}$.

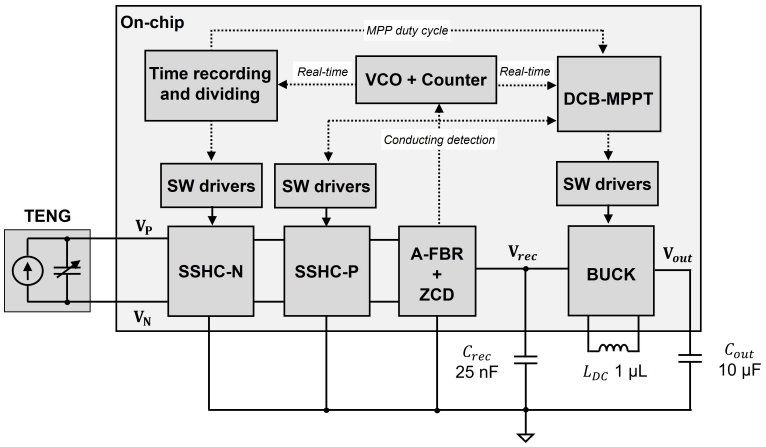

Figure 3.5: The architecture of the proposed triboelectric energy harvester.

work, and the counter is recorded in the register and then reset. In this way, the TENG operation period of the last cycle is measured at the beginning of the new cycle, with $\phi_+ \rightarrow \phi_-$ as the start and end timestamp. The counter and register are imposed of D flip-flop and both have 12 bits, so they can measure and memorize a maximal period of $4096/f_{VCO}$.

Then the recorded period information is utilized in two ways. Assuming that ϕ_+ is equal to ϕ_-, when the transient counter bits are the same to half of the recorded period, the $\phi_- \rightarrow \phi_+$ moment arrives and SSHC-N should be operated. It is implemented by comparing the transient bits of counter to the last 11 bits of the register with 0 at the most significant bit (MSB).

Besides, the recorded operation period can be used to evaluate the MPP state of the rectifier. Since at MPP, the FBR is not conducting in ϕ_- and at least half of ϕ_+, then the 3/4 of the operation time is clipped as the coarse MPP cut-off timestamp. After being added with some calibration bits, the MPP duty cycle is depicted and utilized to track

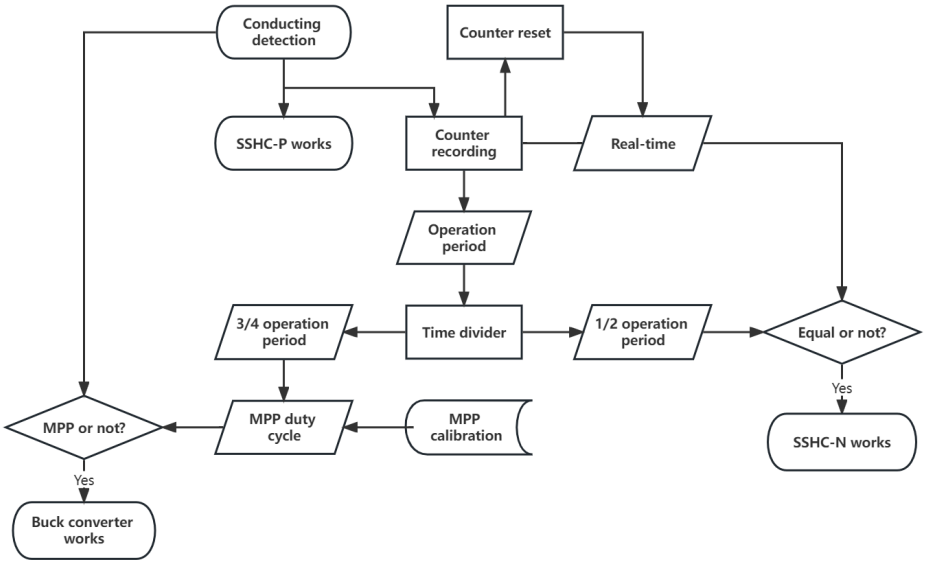

Figure 3.6: The control system workflow of the proposed triboelectric energy harvester.

the MPP state of the rectifier.

The D-SSHC, A-FBR and buck converters are designed and constructed with high-voltage LDMOS, so the harvester can tolerate 70 V for maximum. To suppress the power consumption of the whole system, the control system operates at 1.8 V. The switch drivers (SW drivers) are utilized with level shifters to connect them. The details of significant blocks will be introduced in the following.

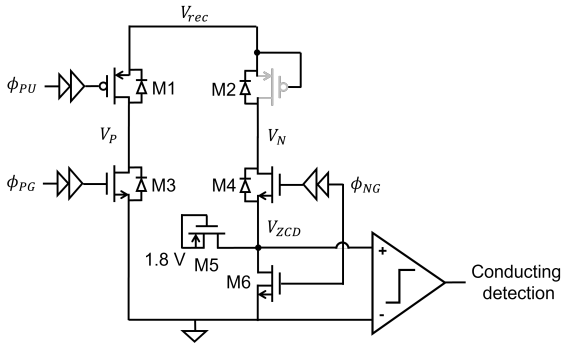

Figure 3.7: The circuit diagram of A-FBR.

3.3.2. ACTIVE FULL BRIDGE RECTIFER WITH ZERO-CURRENT DETECTION

In piezoelectric energy harvesting, the ZCD is implemented with an active diode at the output of the rectifier. However, in triboelectric energy harvesting, the voltage at the V_{rec} is too high to be tolerated by low-voltage devices. Thus we propose an A-FBR with an active diode connected to the ground and isolated from the high voltage. The diagram of the proposed A-FBR is presented in Fig. 3.7. The diodes in M1 - M4 are the body diode of LDMOS, which inherently build up an FBR. M5 and M6 are 5-V PMOS and NMOS respectively. When ϕ_{NG} is in a low voltage level, the gate voltage of M6 is zero, and it operates like a diode with P terminal connected to ground and N terminal connected to V_{ZCD}. In this case, conducting of rectifier can be detected by comparing the V_{ZCD} to the ground. If TENG is in ϕ_+ and the rectifier is conducting, the V_{ZCD} would be lower than 0. Otherwise, the V_{ZCD} is higher than 0. Note that the gate voltage on M4 is 1.8 V when ϕ_{NG} is in a low voltage level to assure V_{ZCD} is higher than 0 V when the rectifier is cut off. When the V_{ZCD} rises to $1.8V - V_{th,LDMOSN}$, M4 is cut off so that the high voltage region is isolated from the low voltage region. However, due to the parasitic capacitors, when V_N increases sharply, V_{ZCD} can increase and exceed the breakdown voltage of devices. Thus the M5 is utilized to limit the voltage at V_{ZCD} under $1.8V + V_{thp}$, so that the V_{ZCD} ranges between $1.8V + V_{thp}$ and $-V_{thn}$, which is why 2-V CMOS is not used here.

In practice, during the cut-off time in ϕ_+, the V_{ZCD} can be a bit lower than 0 as long as the M6 is not conducting. This interrupts the conducting detection. To avoid this situation, ϕ_{PU} is utilized to pull up the V_P to V_{rec} at the end of flip at $\phi_- \rightarrow \phi_+$, so that V_N is mostly higher than 0 when the rectifier is cut off. When the voltage over TENG increases, V_N will drop and the rectifier does not conduct until V_N drops to $-V_{thn}$.

To adapt the input voltage range and compare the V_{ZCD} to ground, a comparator is designed for ZCD. The diagram is presented in Fig.3.8. The comparator works in low power by biasing M1 at weak inversion and assigning long transistors in the second stage (M6 - M9). Besides, M1 - M5 are also designed long to suppress the channel length modulation. Such an unbalanced structure contributes to high gain with low power consumption, but the layout requires extra care to avoid offset.

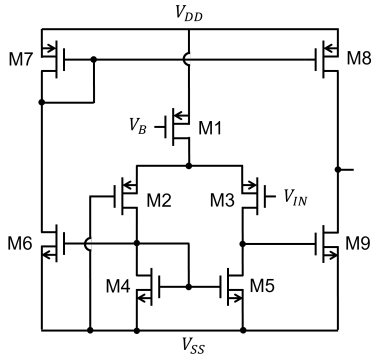

Figure 3.8: The circuit diagram of the comparator used in ZCD.

3.3.3. LOW-POWER VOLTAGE-CONTROLLED OSCILLATOR

Since we use a VCO and a counter to measure and compare the time in a low frequency (< 200 Hz), the operational frequency of the oscillator does not need to be very high. Besides, since the VCO is always working, its power consumption must be suppressed. Therefore, a low-power VCO is proposed in Fig. 3.9. It is based on a ring oscillator but with each inverter clamped by current sources, which are PMOS or NMOS biased by the current reference respectively. Furthermore, the current clamp can suppress leakage current through inverters caused by short circuit.

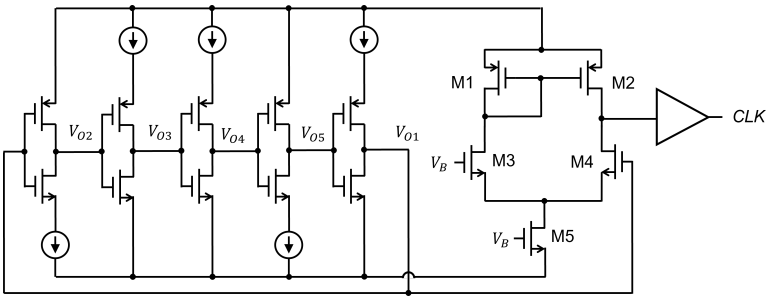

Figure 3.9: The circuit diagram of the VCO.

If not considering the parasitic capacitance in the circuit, the operational frequency of this VCO is 235 kHz, costing around 330 nW. Considering the parasitic capacitance in layout and the effect of corner and temperature, the operational frequency varies between 130 kHz and 200 kHz, while the power consumption ranges from 225 nW to 475 nW. The performance shall be validated in post-simulation in the future. Currently, according to the pre-simulation result, the operational frequency is acceptable for a precise MPPT, and the power consumption is low enough.

3.3.4. SWITCH DRIVER

The level shifter and switch driver are significant parts in this work since they are the connection between the low-voltage control system and high-voltage switches. There are three types of switch drivers implemented for this harvester: level shifter, bootstrap gate driver (BGD), and DC-DC switch driver. The level shifter is the most fundamental one and is employed in the latter two drivers to convert the 1.8-V control signal to 5-V signal. In comparison, the BGD and DC-DC switch driver are more complicated and thus will be elaborated.

BOOTSTRAP GATE DRIVER (BGD)

Since the breakdown voltage between the gate and source of LDMOS is only 5.5 V, a BGD is necessary to drive the LDMOS properly. Fig. 3.10 presents the circuit diagram of the BGD as well as the high-voltage switches (HVS) driven by that. HVS is composed of two LDMOS with source terminals connected to reject leakage current through the body diode. The output node of BGD V_G and V_S is connected to the common gate and source of the HVS respectively. V_G is connected to V_{boot} after providing a pulse to the left input

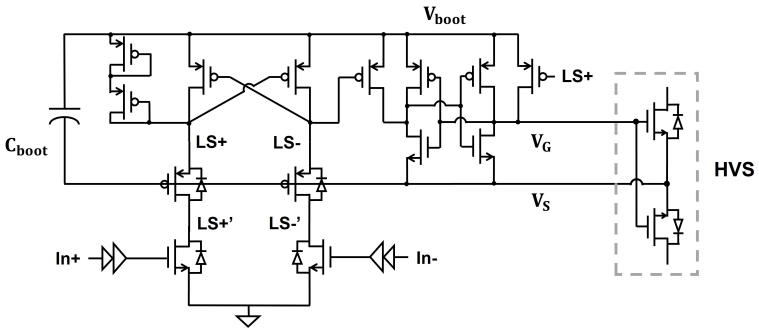

Figure 3.10: The circuit diagram of the bootstrap gate driver (BGD) block and the high-voltage switch (HVS).

node $In+$ and shifted to V_S after providing a pulse to the other input node $In-$. This architecture is advantageous in ultra-low static power consumption and free level shifting between 0 V and 70 V. Most power dissipation in driving this BGD is in charging parasitic capacitors at the node $LS+'$, $LS-'$ from the ground to the bootstrap voltage. In this case, the bootstrap capacitance needs to be customized based on the voltage on the SCs.

DC-DC SWITCH DRIVER

To achieve a smaller form factor, the inductor needs to be small in buck converter. This requires both a fast switching speed and a large switch. A specified switch driver is built for it as presented in Fig. 3.11. The high-voltage region and low voltage-region are separated by two capacitors C_P and C_M. C_P is much larger than C_M since the gate capacitance of power switch is large. When it is going to turn on the power switch, the non-overlapping level shifter assures that $V_{DM,L}$ increases to 5 V first so that the M2 is turned off. Then $V_{DP,L}$ drops to 0 V, with the voltage drop converted to $V_{DP,H}$ through C_P. Due to the large gate capacitance of the power switch, the source-to-gate voltage cannot reach 5 V. Fortunately, according to the simulation, the on-resistance of p-LDMOS will not increase a lot when the current is far lower than the saturation current. In specific, when the current through the power switch is 500 mA, the on-resistance is 3.27Ω, 3.52Ω and 3.93Ω when the source-to-gate voltage of the p-type LDMOS is $5V$, $4V$, and $3V$ respectively. However, the capacitance required for 3-V voltage drop is only half of that for 4-V drop, which saves a large amount of space. With this switch, the inductor employed in this harvester can be as small as $1\mu H$.

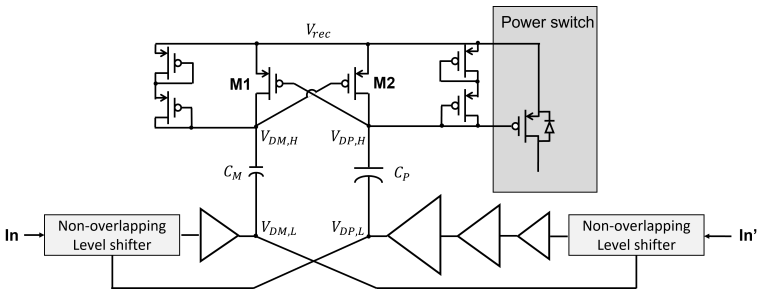

Figure 3.11: The circuit diagram of DC-DC switch driver.

BIBLIOGRAPHY

[1] J. Tillak, S. Akhbari, N. Shah, L. Radakovic, L. Lin, and J. Yoo, "A 2.34j/scan acoustic power scalable charge-redistribution pmut interface system with on-chip aberration compensation for portable ultrasonic applications," in *2016 IEEE Asian Solid-State Circuits Conference (A-SSCC)*, pp. 189–192. DOI: 10.1109/ASSCC.2016.7844167.

[2] X. Yue and S. Du, "Voltage flip efficiency optimization of sshc rectifiers for piezoelectric energy harvesting," in *2021 IEEE International Symposium on Circuits and Systems (ISCAS)*, pp. 1–5, ISBN: 2158-1525. DOI: 10.1109/ISCAS51556.2021.9401330.

[3] L. Liu, Y. Ou, J. Ma, Y. Xie, and Y. Yu, "An inductorless p-sshc piezoelectric energy harvesting integrated system with high flipping efficiency," *Microelectronics Journal*, vol. 125, p. 105 479, 2022, ISSN: 0026-2692. DOI: https://doi.org/10.1016/j.mejo.2022.105479. [Online]. Available: https://www.sciencedirect.com/science/article/pii/S0026269222001124.

[4] M. Pathak and R. Kumar, "Synchronous inductor switched energy extraction circuits for triboelectric nanogenerator," *IEEE Access*, vol. 9, pp. 76 938–76 954, 2021, ISSN: 2169-3536.

4

SIMULATION RESULTS

4.1. D-SSHC RECTIFIER

The relevant simulation results of D-SSHC are presented in this section. The parameters of TENG are depicted in Table. 1.1. A segment of transient voltage over TENG V_{TE} is presented in Fig. 4.1 to show the startup situation of the harvester. Thanks to the ZCD integrated in A-FBR, D-SSHC can work from the beginning and contribute to a short warm-up time to the MPP. The segments of V_{TE} when rectification voltage is 10 V, 30 V, 50 V, and 70 V are presented in Fig. 4.2 to show that D-SSHC works well at any rectification voltage under 70 V. The transient waveform at the flip is zoomed in as presented in Fig. 4.3a and Fig. 4.3b. The maximal flipping efficiency is 78% and 59% respectively. It is noticed that the flip efficiency of SSHC-P is much lower than expected. This is because of the charge loss caused by the parasitic capacitance at the source of HVS. In each cycle, the source of HVS is reset to 0 V to charge the bootstrap capacitor, and during flipping, parasitic capacitors need to be charged from 0 V to the voltage equal to that on flip capacitors. Furthermore, if the flip capacitance and C_{TE} are much larger than the parasitic capacitance, the power loss is negligible. However, the $C_{TE,min}$ is as small as 10 pF and the flip capacitance in SSHC-P is 40 pF for each stage, thus the $\eta_{f,pn}$ degrades severely. Fortunately, due to the small capacitance of $C_{TE,min}$, the $\eta_{f,pn}$ contributes little to the output energy.

In addition, a plot of extracted power versus rectification voltage is derived in Fig. 4.4, including the comparison between the power extracted by D-SSHC and that extracted by ideal-FBR. D-SSHC boosts the extracted power to 5.7 times the peak power output of FBR.

4.2. MPPT

According to Fig. 4.4, the MPP of rectifier for this TENG is at 70 V, thus we cannot observe the performance of the DCB-MPPT. Therefore, we drop the charge density of TENG to test the performance of MPPT block. When the charge density is decreased by 10 times, the MPP voltage is within 70 V and the power input to the harvester (P_{IN}) and the power

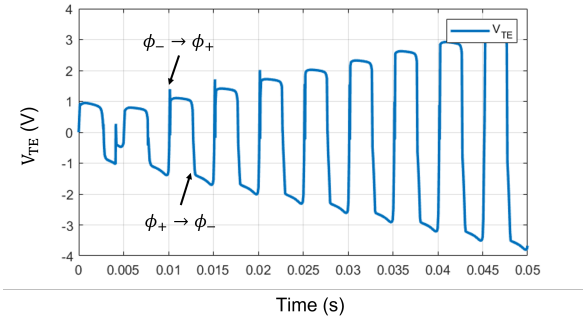

Figure 4.1: The transient waveform of voltage over TENG V_{TE} at the start-up stage.

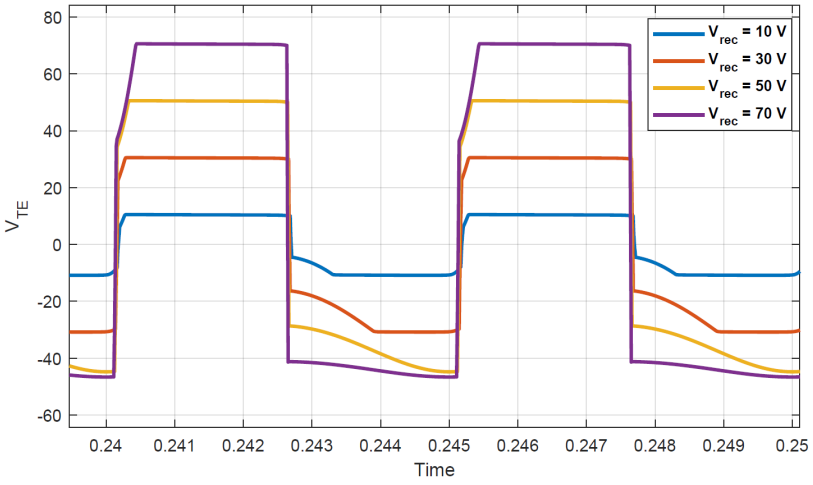

Figure 4.2: The transient waveform of voltage over TENG V_{TE} when the rectification voltage is 10 V, 30 V, 50 V, and 70 V.

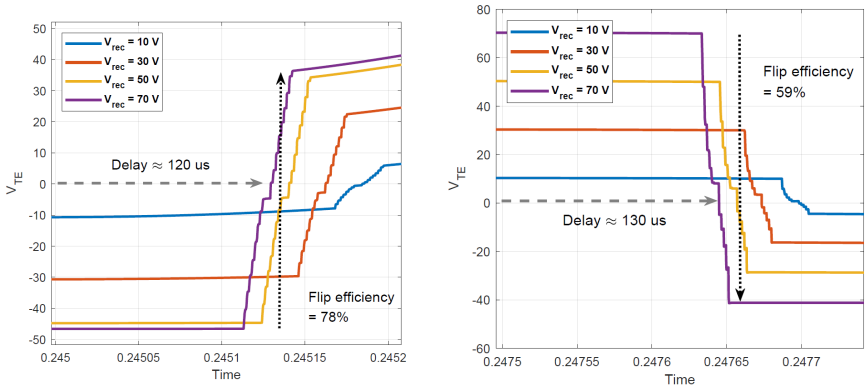

(a) (b)

Figure 4.3: The zoomed-in transient waveform of voltage over TENG V_{TE} at (a) $\phi_- \rightarrow \phi_+$ and (b) $\phi_+ \rightarrow \phi_-$.

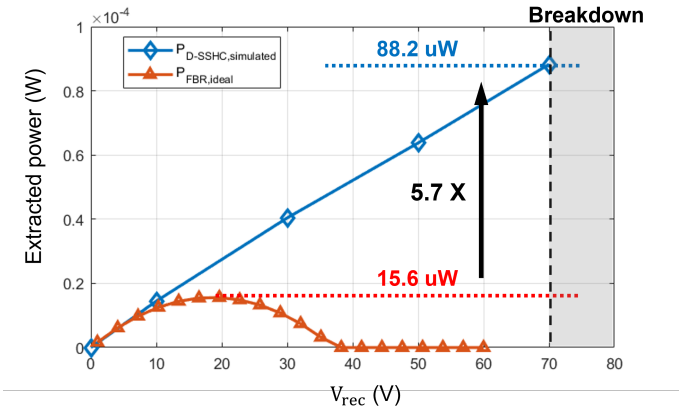

Figure 4.4: Power extracted by D-SSHC and ideal-FBR versus rectification voltage.

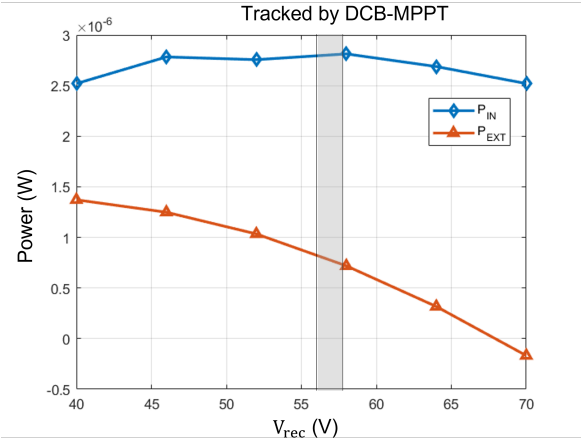

Figure 4.5: The power input to the harvester (P_{IN}) and the power extracted by D-SSHC (P_{EXT}) versus rectification voltage (V_{rec}).

extracted by D-SSHC (P_{EXT}) versus rectification voltage (V_{rec}) is presented in Fig. 4.5. The grey area indicates the rectification voltage maintained by DCB-MPPT block. The MPPT efficiency based on the extracted power is around 50%. This is caused by the A-FBR. Due to the pull-up phase, some charge is transferred from rectification capacitor to the parasitic capacitors in A-FBR and the internal capacitor of TENG. The power dissipation of this process varies from 0 μW to 3 μW, increasing with the increase of rectification voltage. Normally, this power dissipation is much smaller than the power harvested. However, for the TENG whose charge density is small or displacement between electrodes is short, the harvested power is small so the power cost by the parasitic capacitor is significant. However, according to Fig. 4.5, the DCB-MPPT tracks the peak input power precisely, which validates the effectiveness of this MPPT methodology in triboelectric energy harvesting.

4.3. POWER CONSUMPTION

The power breakdown in depicted in the Table.4.1. The power is mainly consumed by the switching loss of DC-DC converter and D-SSHC. The total power consumption is 3.2μW. Based on this result, the end-to-end efficiency when rectification voltage is 70 V and output voltage is 4 V is 65%, with extracted power and output power equal to 88.2μW and 59.3μW respectively. A comparison table is also depicted in Table.4.3. This work achieves the highest energy extraction enhancement (P_{EXT}/P_{FBR}) compared to the state-of-the-arts.

Table 4.1: Power consumption breakdown

Category		Power consumption (nW)	Percentage (%)
D-SSHC	Switch driving	806	26
	Control	44	1
A-FBR	ZCD	101	3
	Switch driving	44	1
DCB-MPPT		226	7
DC-DC buck converter		1430	46
Clock		300	10
Current reference		86	3
Other		92	3
Total		3129	100

Table 4.3: Comparison table

	[1]	[2]	[3]	[4]*	This work*
Transducer	CS-TENG	CS-TENG	Wind-TENG	CS-TENG	CS-TENG
Process	0.18um BCD	0.18um BCD	0.18um BCD	0.18um BCD	0.18um BCD
Rectifier	P-SSHI rectifier	Dual-output rectifier	MCS-BF rectifier	Multi-shot SCE	D-SSHC rectifier
Regulation	BUCK +SCC	Dual-input BUCK	SCC	BUCK-BOOST	BUCK
MPPT	-	FOCV	-	-	DCB-MPPT
$V_{EXT}(V)$	12-70	<70	65*N	<70	<70
PCE	32.70%	75.60%	70.70%	63.28%	67%
Output voltage	2	2.8-3.3	3.1-4.3	2-20	4
$P_{EXT}(\mu W)$	2.95	3.9-10.5	1200	90.3	88.2
FoM (nJ/cm^2)	44	64	380	-	27
P_{EXT}/P_{FBR}	1.62×	-	3.14×	1.91×	5.7×

* Simulated

BIBLIOGRAPHY

[1] I. Kara, M. Becermis, M. A. A. Kamar, M. Aktan, H. Dogan, and S. Mutlu, "A 70-to-2 v triboelectric energy harvesting system utilizing parallel-sshi rectifier and dc-dc converters," *IEEE Transactions on Circuits and Systems I: Regular Papers*, vol. 68, no. 1, pp. 210–223, 2021, ISSN: 1558-0806. DOI: 10.1109/TCSI.2020.3025468.

[2] J. Maeng, I. Park, M. Shim, J. Jeong, and C. Kim, "A high-voltage dual-input buck converter with bidirectional inductor current for triboelectric energy-harvesting applications," *IEEE Journal of Solid-State Circuits*, vol. 56, no. 2, pp. 541–553, 2021, ISSN: 1558-173X. DOI: 10.1109/JSSC.2020.3012991.

[3] J. Lee, S. H. Lee, G. G. Kang, J. H. Kim, G. H. Cho, and H. S. Kim, "A triboelectric energy-harvesting interface with scalable multi-chip-stacked bias-flip and daisy-chained synchronous signaling techniques," *IEEE Journal of Solid-State Circuits*, pp. 1–15, 2022, ISSN: 1558-173X. DOI: 10.1109/JSSC.2022.3193738.

[4] M. Pathak, S. Xie, C. Huang, and R. Kumar, "High-voltage triboelectric energy harvesting using multi-shot energy extraction in 70-v bcd process," *IEEE Transactions on Circuits and Systems II: Express Briefs*, vol. 69, no. 5, pp. 2513–2517, 2022, ISSN: 1558-3791. DOI: 10.1109/TCSII.2022.3160676.

5

CONCLUSION

A triboelectric nanogenerator (TENG) is a new mechanical energy transducer that performs high-efficiency energy harvesting from low-frequency and irregular mechanical motion; thus it has wide application scenarios, from biological motion energy harvesting to tide energy harvesting. Due to its different characteristics from those of prior transducers, specific energy harvesting interface circuits need to be designed to achieve high conversion efficiency. This thesis firstly summarizes TENG energy harvesting requirements and recent advancements in triboelectric energy harvesting techniques. Due to the small and time-varying internal capacitance, TENG can generate asymmetric high-voltage output, which is the biggest obstacle in extracting energy harvested by TENGs. Fortunately, some mature methodologies employed in piezoelectric and electrostatic energy harvesting systems have been demonstrated feasible and advantageous in triboelectric energy harvesting. Passive converters take advantage of simplicity and, thus, are widely employed in triboelectric rectification. Active rectifiers such as synchronized electric charge extraction (SECE) rectifiers and synchronous switch harvesting rectifiers are effective in improving the performance of energy extraction from TENG by eliminating the phase difference between the voltage and current outputs. The state-of-the-arts are summarized in one table, with their performance quantified.

Another significant part of this thesis is to propose a new 70-V SSHC recitifer with duty-cycle-based MPPT (DCB-MPPT). It eliminates the phase difference between voltage and current output of TENG with a fully-integrated D-SSHC technique. Besides, to track the MPP of some low-power TENG, a DCB-MPPT is employed to avoid the obstacle and power loss in measuring the open-circuit voltage of TENG. This harvester achieves 65% end-to-end efficiency and 5.3 times enhancement in energy extraction. The power consumption of this harvester is 3.2 μW only. However, the result is simulated but not measured. We will keep working on this harvester and fabricate it on April.

APPENDIX: MPP CUT-OFF DUTY CYCLE CALCULATION

It has been known that the theoretical MPP voltage for bias-flip interface in triboelectric energy harvesting is [1]:

$$V_{rec,mpp} = V_{OC,max}\frac{1+\eta_{f,np}}{2(1-\eta_{f,pn}\eta_{f,np})} = KV_{OC,max}; \tag{1}$$

which is assumed to be the initial voltage over TENG at the beginning of a cycle, right before the $\phi_+ \rightarrow \phi_-$. The cycle is imposed of $\phi_+ \rightarrow \phi_-$, ϕ_-, $\phi_- \rightarrow \phi_+$, and ϕ_+. After the first flip $\phi_+ \rightarrow \phi_-$, the current voltage $V_{TE,1}$ is equal to

$$V_{TE,1} = \eta_{f,pn}V_{rec,mpp}; \tag{2}$$

Then, assuming that no current flows out of the TENG in ϕ_-, the voltage at the end of ϕ_- is

$$V_{TE,2} = \frac{C_{TE,min}V_{TE,1} + Q_{SC}}{C_{TE,max}}; \tag{3}$$

where Q_{SC} represents the amount of charge output by the equivalent current source in TENG every half cycle, which is identical to $C_{TE,min}V_{OC,max}$. The other flip $\phi_- \rightarrow \phi_+$ follows so that the initial voltage at the beginning of ϕ_+ is

$$V_{TE,3} = \eta_{f,np}V_{TE,2} \tag{4}$$

$$= \eta_{f,np}(\eta_{f,pn}K+1)V_{OC,max}\frac{C_{TE,min}}{C_{TE,max}} \tag{5}$$

At this moment, the distance between electrodes is at a minimum. Then in ϕ_+, the distance increases, resulting in voltage V_{OC} increase and capacitance C_{TE} decrease. The real-time voltage over TENG $V_{TE}(t)$ can be calculated by

$$V_{TE}(t) = \frac{V_{TE,3}C_{TE,max}}{C_{TE}(t)} + V_{OC}(t); \tag{6}$$

where

$$V_{OC}(t) = \frac{\sigma x(t)}{\epsilon_0}; \quad C_{TE}(t) = \frac{\epsilon_0 S}{x_0 + x(t)}; \tag{7}$$

x_0 is the effective thickness of dielectric layers. Note that it can be derived that

$$V_{OC,max} = \frac{\sigma x_{max}}{\epsilon_0}; \quad C_{TE,min} = \frac{\epsilon_0 S}{x_0}; \quad C_{TE,max} = \frac{\epsilon_0 S}{x_0 + x_{max}}; \tag{8}$$

When the voltage over TENG is lower than rectification voltage, the rectifier is cut off. Thus at the ending time of the cut-off state (t_{CO}), there is

$$V_{TE}(t_{CO}) = V_{rec,mpp}; \tag{9}$$

It can be substituted and simplified to

$$\frac{x(t_{CO})}{x_{max}} = K - (K\eta_{f,pn}\eta_{f,np} + \eta_{f,np})\frac{x_0 + x(t_{CO})}{x_0 + x_{max}}; \tag{10}$$

Normally, the effective thickness of dielectric layers is much smaller (more than 8 times) than the displacement. Thus the equation can be approximated to

$$\frac{x(t_{CO})}{x_{max}} \approx K - (K\eta_{f,pn}\eta_{f,np} + \eta_{f,np})\frac{x(t_{CO})}{x_{max}}(1+\delta); \quad \delta = \frac{x_0}{x_{max}}; \tag{11}$$

After substitution and simplification, there obtains

$$\frac{x(t_{CO})}{x_{max}} = \frac{1}{2 - \eta_{f,pn}\eta_{f,np} + \delta(\eta_{f,pn}\eta_{f,np} + \frac{\eta_{f,np}}{K})}; \tag{12}$$

Assume that TENG operates in sinusoidal vibration with a frequency of f_{TE}, then it is derived that

$$\frac{x(t)}{x_{max}} = \frac{1}{2}(1 - \cos 2\pi f_{TE} t) \tag{13}$$

$$D_{CO} = f_{TE} t_{CO} = \frac{1}{2\pi}\arccos\frac{-\eta_{f,pn}\eta_{f,np} + \delta(\eta_{f,pn}\eta_{f,np} + \frac{\eta_{f,np}}{K})}{2 - \eta_{f,pn}\eta_{f,np} + \delta(\eta_{f,pn}\eta_{f,np} + \frac{\eta_{f,np}}{K})} \tag{14}$$

where D_{CO} denotes the cut-off duty cycle. δ is normally smaller than 0.2, and K is larger than 1. In convenience, a simpler approximate expression can be obtained as

$$D_{CO} = \frac{1}{2\pi}\arccos\frac{-\eta_{f,pn}\eta_{f,np}}{2 - \eta_{f,pn}\eta_{f,np}}; \tag{15}$$

LIST OF PUBLICATIONS

1. **W. Peng**, S. Du, The Advances in Conversion Techniques in Triboelectric Energy Harvesting: a Review, *Transactions on Circuits and Systems I: Regular Papers* (revision submitted)